AGU PUBLICATIONS

JGR

Journal of Geophysical Research: Solid Earth

RESEARCH ARTICLE
10.1002/2015JB011885

Key Points:
- We have created a new model for mid-ocean ridge melting
- Model can reproduce global MORB geochemistry
- Melts are transported to the ridge over short length scales

Supporting Information:
- Text S1
- Script S1
- Script S2
- Script S3
- Figure S1
- Figure S2

Correspondence to:
M. D. Behn,
mbehn@whoi.edu

Citation:
Behn, M. D., and T. L. Grove (2015), Melting systematics in mid-ocean ridge basalts: Application of a plagioclase-spinel melting model to global variations in major element chemistry and crustal thickness, *J. Geophys. Res. Solid Earth*, *120*, 4863–4886, doi:10.1002/2015JB011885.

Received 12 JAN 2015
Accepted 29 MAY 2015
Accepted article online 1 JUN 2015
Published online 20 JUL 2015

©2015. American Geophysical Union. All Rights Reserved.

Melting systematics in mid-ocean ridge basalts: Application of a plagioclase-spinel melting model to global variations in major element chemistry and crustal thickness

Mark D. Behn[1] and Timothy L. Grove[2]

[1]Department of Geology and Geophysics, Woods Hole Oceanographic Institution, Woods Hole, Massachusetts, USA, [2]Department of Earth, Atmospheric, and Planetary Science, Massachusetts Institute of Technology, Cambridge, Massachusetts, USA

Abstract We present a new model for anhydrous melting in the spinel and plagioclase stability fields that provides enhanced predictive capabilities for the major element compositional variability found in mid-ocean ridge basalts (MORBs). The model is built on the formulation of Kinzler and Grove (1992) and Kinzler (1997) but incorporates new experimental data collected since these calibrations. The melting model is coupled to geodynamic simulations of mantle flow and mid-ocean ridge temperature structure to investigate global variations in MORB chemistry and crustal thickness as a function of mantle potential temperature, spreading rate, mantle composition, and the pattern(s) of melt migration. While the initiation of melting is controlled by mantle temperature, the cessation of melting is primarily determined by spreading rate, which controls the thickness of the lithospheric lid, and not by the exhaustion of clinopyroxene. Spreading rate has the greatest influence on MORB compositions at slow to ultraslow spreading rates (<2 cm/yr half rate), where the thermal boundary layer becomes thicker than the oceanic crust. A key aspect of our approach is that we incorporate evidence from both MORB major element compositions and seismically determined crustal thicknesses to constrain global variations in mantle melting parameters. Specifically, we show that to explain the global data set of crustal thickness, Na_8, Fe_8, Si_8, Ca_8/Al_8, and K_8/Ti_8 (oxides normalized to 8 wt % MgO) require a relatively narrow zone over which melts are pooled to the ridge axis. In all cases, our preferred model involves melt transport to the ridge axis over relatively short horizontal length scales (~25 km). This implies that although melting occurs over a wide region beneath the ridge axis, up to 20–40% of the total melt volume is not extracted and will eventually refreeze and refertilize the lithosphere. We find that the temperature range required to explain the global geochemical and geophysical data sets is 1300°C to 1450°C. Finally, a small subset of the global data is best modeled as melts of a depleted mantle source composition (e.g., depleted MORB mantle—2% melt).

1. Introduction

Mid-ocean ridges are the primary location of volcanism on Earth. Magma generated by decompression of the upwelling mantle beneath a ridge axis creates the oceanic crust, and the heat associated with magma emplacement drives biological activity and hydrothermal circulation, which in turn modulates chemical exchange between the oceans and the lithosphere. The volume and composition of melts formed at mid-ocean ridges are controlled by a range of parameters, including mantle potential temperature, spreading rate, mantle composition, and the patterns and length scales of melt migration in the mantle [e.g., *Reid and Jackson*, 1981; *Klein and Langmuir*, 1987; *McKenzie and Bickle*, 1988; *Niu and Batiza*, 1991; *Langmuir et al.*, 1992; *Kinzler and Grove*, 1992a, 1992b, 1993; *Plank and Langmuir*, 1992; *White et al.*, 1992, 2001; *Plank et al.*, 1995; *Asimow et al.*, 2001]. Melt compositions are further modified by fractional crystallization and melt-wall rock interaction as melts pass through the thermal boundary layer [e.g., *Langmuir*, 1989; *Grove et al.*, 1992; *Spera and Bohrson*, 2001; *Rubin and Sinton*, 2007; *Lissenberg and Dick*, 2008; *O'Neill and Jenner*, 2012]. The observed composition of mid-ocean ridge basalts (MORBs) therefore provides a record of these processes and can be used to infer the conditions under which melts are produced in the mantle and transported to the ridge axis.

A common approach for extracting information on these processes is to compare observed MORB compositions to forward predictions of mantle melting. Studies that couple models of mantle flow and

temperature structure with thermodynamic parameterizations can predict not only compositional variability but also spatial and temporal variations in crustal thickness, which can be compared to seafloor geophysical data sets. This methodology has been used to place first-order constraints on the parameters that control crustal thickness and the compositional variability of mid-ocean ridge basalts [e.g., *Cordery and Phipps Morgan*, 1992; *Shen and Forsyth*, 1995; *Asimow et al*., 2001; *Gregg et al*., 2009; *Shaw et al*., 2010; *Montési et al*., 2011]. However, there remains a surprising degree of uncertainty in the factors that control melting at mid-ocean ridges. For example, while the relationship between crustal thickness and spreading rate at ridge segments not influenced by hot spots is well known from seismic surveys [e.g., *White et al*., 2001], it has proven difficult to reproduce these data using existing geodynamic models for either passive or buoyancy-driven flow [e.g., *Braun et al*., 2000]. Moreover, while crustal thickness and MORB chemistry have been used jointly to place constraints on melting parameters such as mantle temperature and the thickness of the lithospheric lid [e.g., *Klein and Langmuir*, 1987], there remains considerable debate over the magnitude of the mantle temperature variations beneath ridges not affected by hot spots, with estimates ranging from 100°C to 300°C [*Putirka et al*., 2007; *Herzberg et al*., 2007; *Herzberg and Asimow*, 2008; *Lee et al*., 2009; *Dalton et al*., 2014]. Constraining these variations is further complicated by the fact that the initiation of melting and melt productivity as a function of depth can be influenced by a number of factors including the presence of volatiles [e.g., *Asimow and Langmuir*, 2003; *Katz et al*., 2003; *Asimow et al*., 2004; *Cushman et al*., 2004]. Finally, the efficiency of melt extraction (particularly at low melt fractions), the length scales and mechanisms by which melt is focused to the ridge axis, and the relative contributions of high-pressure crystallization are poorly constrained. Taken altogether, these variables limit our ability to interpret the compositional variability preserved in MORB.

To address these issues and better constrain the melting process beneath mid-ocean ridges, we present a new model for MORB melting built on the formulation of *Kinzler and Grove* [1992a, 1992b, 1993] and *Kinzler* [1997], which incorporates new experimental data collected since the KG92 calibration [e.g., *Till et al*., 2012]. Our new model (referred to hereafter as BG15) provides parameterizations for the pressure dependence of alkali partitioning between melt and pyroxene and the pressure sensitivity of the melting reaction. BG15 is devised to handle anhydrous melting in the plagioclase-spinel melting regime. However, it is also designed in a flexible open-source manner to facilitate the incorporation of additional melting phenomenon (e.g., hydrous melting or melting in the garnet stability field) in the future. The model is coupled to 2-D geodynamic calculations of the mantle flow field and temperature structure for mid-ocean ridges to investigate the competing effects of mantle potential temperature, mantle composition, spreading rate, and the geometry of the melting region on melt composition. In addition, we explore calculations with both constant and variable melt productivity as a function of pressure. These forward calculations are compared to recent compilations of MORB geochemical data [*Gale et al*., 2013, 2014] and seismic determinations of on-axis oceanic crustal thickness. The co-located data sets provide key constraints, which allow us to infer global variations in mantle temperature along with other MORB melting variables (e.g., mantle depletion and shape of the melting regime). Finally, to facilitate the use of our model in future studies of MORB melting, we provide the model as a series of MATLAB® scripts with several example applications.

2. A New Model for MORB Melting

While several empirical melting models have been developed to study mid-ocean ridge melting systematics [e.g., *Langmuir et al*., 1992; *Niu and Batiza*, 1991, 1993], the two most widely used thermodynamically based models for simulating the full range of major element compositional variability during MORB melting are *Kinzler and Grove* [1992a, 1992b, 1993] (hereafter referred to as KG92) and (p)MELTS [*Asimow et al*., 1997, 2001]. KG92 is a model for nominally anhydrous melting constrained by experimental data over a relatively narrow range of melting conditions expected beneath mid-ocean ridges. By contrast, MELTS utilizes a thermodynamically self-consistent approach that relates equilibrium mineral phases to thermodynamic state variables (e.g., entropy and enthalpy). By minimizing the enthalpy of the system at a given pressure, entropy, and bulk composition, MELTS can be used to predict melt and residue compositions as well as the melt productivity and temperature during decompression melting [*Asimow et al*., 1997, 2001]. MELTS is thus a powerful tool for modeling melts derived from a wide range of mantle source compositions (major, trace, and volatile) and for assessing how varying specific parameters will influence melt composition.

However, the versatility of MELTS also means that for specific applications, it can be less accurate than more specialized models. For example, it has been shown that for peridotite partial melting, KG92 is typically more accurate in predicting melt fraction, composition, and temperature [e.g., *Robinson et al*., 1998; *Hirschmann et al*., 1998; *Gaetani*, 1998]. Such discrepancies are critical when trying to use forward calculations of melting from geodynamic models to constrain melting parameters (mantle potential temperature, mantle composition, and melt migration patterns) that produce compositions observed in a specific ridge environment. Yet while KG92 has been shown to be more accurate than MELTS for predicting MORB compositions, it is based on an experimental data set that is more than 20 years old. Specifically, it does not account for the pressure dependence of alkali partitioning between melt and orthopyroxene and clinopyroxene or the pressure sensitivity of the melting reaction. New experimental data collected since the KG92 calibration allow us to better constrain these effects, as well as melting over a broader range of mantle source compositions. Below we describe the formulation of our new melting model and illustrate how it compares with KG92 and MELTS for a series of simple melting scenarios.

2.1. Parameterization of Melting Equilibria

The BG15 melting model developed here is built on the formulations of KG92, *Kinzler* [1997], and *Till et al*. [2012]. The approach uses an adaptation of the Gibbs method [*Spear et al*., 1982], in which three sets of equations constrain the composition and proportions of phases in equilibrium during a heterogeneous reaction. The first is mass balance, which states that the mass of an element in each phase must sum to the mass of that element in the bulk composition:

$$\Sigma_j n_j {x_j}^i = {x_{\text{bulk}}}^i \tag{1}$$

where n_j is the weight fraction of phase j, x_j^i is the weight percent of element i in phase j, and ${x_{\text{bulk}}}^i$ is the weight percent of element i in the bulk composition.

The second constraint is that each phase must be stoichiometric:

$$\Sigma_i {x_j}^i = 1 \tag{2}$$

where the summation is over all elements i in phase j.

The third constraint is the equilibrium condition, stating that the partial molar Gibbs free energy (μ) of each component in each phase in equilibrium must be equal:

$${\mu^i}_a = {\mu^i}_b = {\mu^i}_c = {\mu^i}_d \ldots .. = {\mu^i}_n \tag{3}$$

In the KG92 adaptation of the Gibbs method to mantle melting, equation (3) is represented by a melting reaction between the solid and liquid phases that predicts the composition of the melt in equilibrium with those solid phases at a specified extent of melting. Mineral components are used to describe the composition of a mantle melt in equilibrium with either spinel or plagioclase lherzolite. Mass balance (equations (1) and (2)) is maintained by subtracting the predicted melt composition from the bulk mantle and then adjusting the proportions of the remaining solid phases in the mantle using the stoichiometric coefficients of pressure-dependent melting reactions.

By specifying a sufficient number of compositional and intensive variables we calculate melts of a natural mantle peridotite system over a range of pressure (P), temperature (T), and compositional space. Following the Gibbs phase rule, the variance (**F**) of any such system is defined as $\mathbf{F} = c + 2 - \Phi$, where c is the number of chemical components and Φ is the number of phases [*Spear*, 1993]. In general, for melting of spinel and plagioclase lherzolite, the melting equilibrium involves five phases: melt, olivine, orthopyroxene, high-Ca clinopyroxene, and an aluminous phase (here spinel or plagioclase). In the four-component CaO-MgO-Al_2O_3-SiO_2 system, the melting reactions are therefore univariant ($\mathbf{F} = 1$), and the melt composition and temperature can be determined assuming that only pressure is specified. Over a short interval the system contains both plagioclase and spinel, but we have not explicitly incorporated this stability region into our model, because the pressure interval where it occurs is small (<1 kbar [*Till et al*., 2012]). Further, in our approximation, if plagioclase is exhausted during late-stage, low-pressure melting, BG15 continues to use the plagioclase lherzolite model. BG15 does not model melt evolution after exhaustion of cpx. For natural peridotite systems it has been shown that additional chemical components involving TiO_2, K_2O, Na_2O, Mg#, and Cr# are important

and influence the composition of liquids in equilibrium with lherzolite mineral assemblages [e.g., *Kushiro*, 1975; *Kinzler and Grove*, 1992a; *Walter and Presnall*, 1994]. To address this, we follow *Till et al*. [2012] and choose 1-Mg# (molar units), NaK# ([$Na_2O + K_2O$]/[$Na_2O + K_2O + CaO$] calculated in wt % units), TiO_2 (wt %), and K_2O (wt %) as our compositional variables. We note that although Cr# is not considered as a compositional variable, Cr_2O_3 partitioning is tracked between spinel and the melt (see below). Fixing pressure thus allows us to solve the four-component, five-phase system in pressure-temperature-composition space. The composition of the spinel and plagioclase lherzolite melts are expressed in terms of pseudoquaternary mineral components: olivine, clinopyroxene, plagioclase, and quartz [*Tormey et al*., 1987; *Grove*, 1993], and the expressions for melt composition and temperature as a function of pressure and the four primary compositional variables are derived by multiple linear regression [*Till et al*., 2012].

2.2. Application to Decompression Melting in the Upper Mantle

We apply this approach to the mid-ocean ridge environment by considering melting along pressure-temperature paths appropriate for the ascending mantle while correcting for the effects of the latent heat of melting. In this study, we investigate scenarios in which the *P-T* path follows a specific mantle adiabat, as well as cases in which the *P-T* path is determined from numerical models that incorporate conductive cooling from the surface, and temperature- and stress-dependent viscosity of the mantle. Based on the mantle source composition, the initial mantle mode is recalculated to the high-pressure, high-temperature assemblage that would be stable on the solidus. Under these conditions, the high-Ca pyroxene is a subcalcic augite, which significantly increases the abundance of cpx over opx in the solid assemblage [*Till et al*., 2012]. For an initial (premelting), *P-T* path melting is then calculated in the following steps:

Step 1: Calculate composition of melt in equilibrium with the mantle. Nonmodal batch melting is used to calculate the concentration of major element oxides TiO_2, Na_2O, K_2O, and Cr_2O_3 in a melt in equilibrium with the mantle. We incorporate a pressure-dependent melting reaction calibrated between 0.1 and 2.4 GPa [*Kinzler*, 1997; *Kinzler and Grove*, 1999] and a pressure-dependent model for the partitioning of Na_2O and TiO_2 between high-Ca clinopyroxene and orthopyroxene and melt [*Till et al*., 2012] (Figure S1 in the supporting information). In these calculations the plagioclase-spinel phase transition is assumed to be invariant and to occur at 0.9 GPa. The Mg# of the melt is calculated by mass balance of MgO and FeO following the approach of KG92 assuming pressure-dependent mineral melt exchange coefficients (Fe-Mg $K_D^{min/melt}$). Expressions for $K_D^{olv/melt}$, $K_D^{cpx/melt}$, and $K_D^{opx/melt}$ derived from experimental data are shown in Figure S2 in the supporting information. (Note that there is insufficient experimental evidence to support a pressure dependence for $K_D^{sp/melt}$; thus, we assign a constant value of 0.6.) The NaK# of the melt is calculated by making an additional estimate of the CaO content of the melt. Once these major element oxides are determined, they are recast in terms of the four primary compositional variables: 1-Mg#, NaK#, TiO_2, and K_2O.

Step 2: Calculate solidus temperature and pseudoquaternary mineral components of the melt. Based on the four primary compositional variables and pressure, we then use the expressions from *Till et al*. [2012] to calculate the pseudoquaternary mineral components of the melt (olivine, clinopyroxene, plagioclase, and quartz) and the solidus temperature. Here we approximate the solidus as the four-phase saturation temperature.

Step 3: Check for melting. The temperature on the mantle ascent path is then compared to the calculated solidus temperature to determine whether melting has occurred. If melting occurs, we preceed to Step #4. If melting does not occur, we return to Step #1 and recalculate the composition of the equilibrium melt at the next pressure increment along the ascent path.

Step 4: Transform pseudoquaternary mineral components and compositional variables into weight percent oxide description of melt composition. Following the approach of KG92 we calculate SiO_2, TiO_2, Al_2O_3, Cr_2O_3, FeO, MgO, CaO, K_2O, and Na_2O (in weight percent) of the incremental melt from the four pseudoquaternary mineral components and the four compositional variables.

Step 5: Update composition of residue mantle. Assuming incremental batch melting, the melt derived in Step #4 is used to update the composition of the residue mantle and the mantle mode is adjusted based on the pressure-dependent melting reactions. The total melt removed in each increment is determined by the pressure step, the assumed melt productivity (dF/dP), and the melt fraction removed at each step (assumed to be 90% unless otherwise specified). The pooled melt is calculated as the average of the incremental melts weighted by the melt production rate at each pressure step. The melt production rate

is equivalent to the product of the melt productivity and the upwelling velocity (U_z), the latter of which can be determined from numerical models.

Step 6: Correct temperature for latent heat of melting. Based on the melt fraction at each step, temperature is corrected according to [*Turcotte*, 1982] $\Delta T = \frac{FL}{C_p}$, where ΔT is the temperature reduction due to melting, L is the latent heat of melting (400×10^3 J kg^{-1}), and C_P is the heat capacity (1.25×10^3 J kg^{-1} K^{-1}).

The steps described above are iterated along the mantle ascent path until melting is terminated by the overlying lithosphere. The corrected temperature from Step #6 is used to check for melting at the next interval along the ascent path (Step #3).

In addition to using the recalibrated spinel and plagioclase melting relations of *Till et al*. [2012], this model differs from KG92 in several important regards. First, we incorporate a pressure-dependent melting reaction [*Kinzler*, 1997], pressure-dependent partitioning of alkalis between pyroxene and melt, and pressure-dependent Fe-Mg exchange coefficients. The effects of pressure on the melting reaction in the spinel field are significant. Melting is peritectic with orthopyroxene on the melt side of the reaction at pressures $>$1.6 GPa switching to olivine on the melt side at $<$1.6 GPa (Figure S1c in the supporting information). The change in compatibility of Na in clinopyroxene with increasing pressure exercises an important control on the melt composition (Figure S1a in the supporting information). Second, we calculate partitioning of Cr_2O_3 between spinel and the melt, allowing us to evaluate the Cr# of the mantle residue. Finally, we incorporate different parameterizations for melt productivity as a function of pressure. KG92 assumed a constant melt productivity ($dF/dP = 1\%$ kbar^{-1}) during decompression melting. However, calculations of isentropic melting based on thermodynamic modeling suggest that melt productivity is strongly pressure dependent [*Asimow et al*., 1997, 2001]. Both parameterizations for melt productivity are tested, and their effects on melt compositions are discussed in detail below.

The MATLAB® code used for the calculations presented in this study is included in the online supporting information. In addition, several example scripts are provided to illustrate how the BG15 model can be used to simulate both isobaric melting and melting along a 1-D mantle adiabat.

2.3. Coupling Melting With Geodynamic Models for Mantle Flow and Temperature

In order to make specific predictions of MORB chemistry in different spreading environments, we use geodynamic simulations to predict the temperature structure beneath a mid-ocean ridge from which melting is subsequently calculated. Mantle temperature and mantle flow are calculated using COMSOL Multiphysics assuming a visco-plastic temperature-dependent rheology that simulates brittle weakening within the lithosphere [*Chen and Morgan*, 1990; *Behn et al*., 2007] and an adiabatic gradient of 1.5°C kbar^{-1}. Compared to a constant or temperature-dependent-only viscosity, the visco-plastic rheology promotes enhanced upwelling directly beneath the ridge axis, which has been shown to reproduce the thermal structure of oceanic transform faults [*Behn et al*., 2007; *Roland et al*., 2010], melt focusing at intratransform spreading centers [*Gregg et al*., 2009], and crustal thickness variations along the ultraslow-spreading Southwest Indian Ridge [*Montési et al*., 2011]. Steady state solutions are derived for a range of spreading half rates ($U = 0.5$–10 cm/yr) and mantle potential temperatures ($T_M = 1300$–1450°C). An example calculation for a half rate of 4 cm/yr, a mantle potential temperature of 1350°C, and a constant melt productivity of 1% kbar^{-1} is shown in Figure 1.

Based on the resulting temperature structure, we then calculate the melt fraction (white lines in Figure 1a) and incremental melt compositions (Figures 1c and 1d) at all points in the model domain while adjusting the temperatures for the removal of latent heat (Figure 1a). To determine the composition of the aggregate melt erupted at the ridge axis, we assume that melts rise vertically through the mantle until they encounter a permeability barrier (e.g., top of the melting region, base of the lithosphere, and cpx-out reaction zone) and then migrate laterally "uphill" along this boundary until they are extracted at the ridge axis [*Sparks and Parmentier*, 1991; *Sparks et al*., 1993; *Magde and Sparks*, 1997; *Ghods and Arkani-Hamed*, 2000]. The assumption of vertical melt migration in the asthenosphere is justified by scaling relations that show that melt buoyancy should dominate over the influence of mantle pressure gradients on melt migration unless the mantle viscosity exceeds ~10^{19} Pa s [e.g., *Spiegelman and McKenzie*, 1987; *Phipps Morgan*, 1987; *Montési et al*., 2011], which is unlikely for the subridge mantle [*Hirth and Kohlstedt*, 2003]. The aggregate melt composition is calculated by pooling all incremental melts and weighting them by the melt production rate (Figure 1b). Note that the stress- and temperature-dependent viscosity predicts

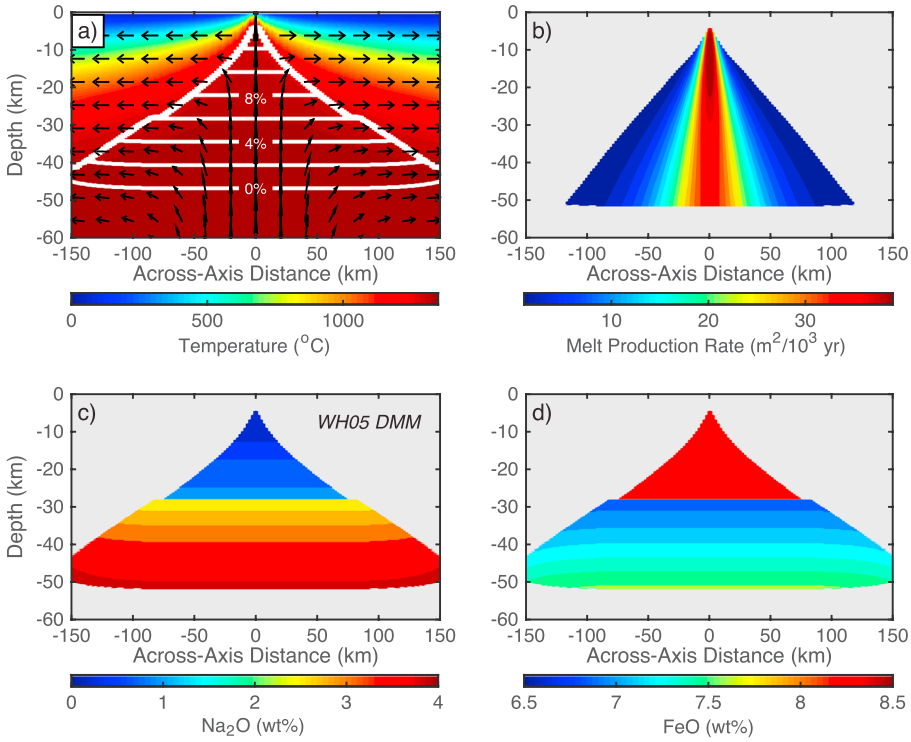

Figure 1. Numerical simulations of mantle flow, temperature, and melting for a spreading half rate of 3 cm/yr and a mantle potential temperature of 1350°C with an adiabatic gradient of 1.5°C kbar^{-1}. (a) Temperature after correction for latent heat of melting, (b) melt production rate, and the (c) Na_2O and (d) FeO contents of the incremental melts. The white contours in Figure 1a illustrate the extent of melting; the black arrows denote the mantle flow field. Calculations assume the DMM composition of *Workman and Hart* [2005].

variable upwelling rates beneath the ridge axis, which map into variations in the melt production rate. Thus, by weighting the incremental melt compositions by the melt production rate predicted from our models, the aggregate melt composition differs in important ways from calculations that assume a uniform upwelling rate beneath the ridge. Similarly, crustal thickness is calculated by integrating the melt production rate and dividing by the spreading rate [*Forsyth*, 1993].

A key parameter in calculating crustal thickness and pooled melt compositions is the length scale over which melts migrate laterally once they encounter the permeability barrier. This length scale is particularly important at intermediate- to fast-spreading ridges, where significant melt fractions are predicted to extend a hundred kilometers or more off axis [e.g., *Toomey et al.*, 1998; *Key et al.*, 2013]. Several recent studies have suggested that not all melt generated off axis is efficiently transported to the axis and that a significant fraction could be lost due to refreezing in the lithosphere [e.g., *Ghods and Arkani-Hamed*, 2000; *Hebert and Montési*, 2010; *Montési et al.*, 2011; *Katz and Weatherley*, 2012; *Wanless et al.*, 2014]. Because melt formed off axis is produced by lower average degrees of melting compared to those generated on axis (Figure 1), the maximum length scale over which melts are transported to the ridge axis strongly influences the pooled melt composition [e.g., *Gregg et al.*, 2009; *Wanless et al.*, 2014]. Moreover, the efficiency of melt extraction also influences the calculated crustal thickness as melts refrozen in the lithosphere will not contribute to the on-axis crustal thickness. We evaluate these effects in a subset of calculations by imposing a maximum horizontal distance over which the melts can be transported to the ridge axis.

2.4. Fractional Crystallization

The final step in modeling the compositional evolution of MORBs is to account for fractional crystallization in the oceanic crust and/or lithosphere after melting ceases at the top of the asthenosphere. Following *Gregg et al.* [2009], we use the model of *Yang et al.* [1996] to calculate fractional crystallization of the pooled melts at pressures below which melting ceases. This is an important predictive characteristic of our

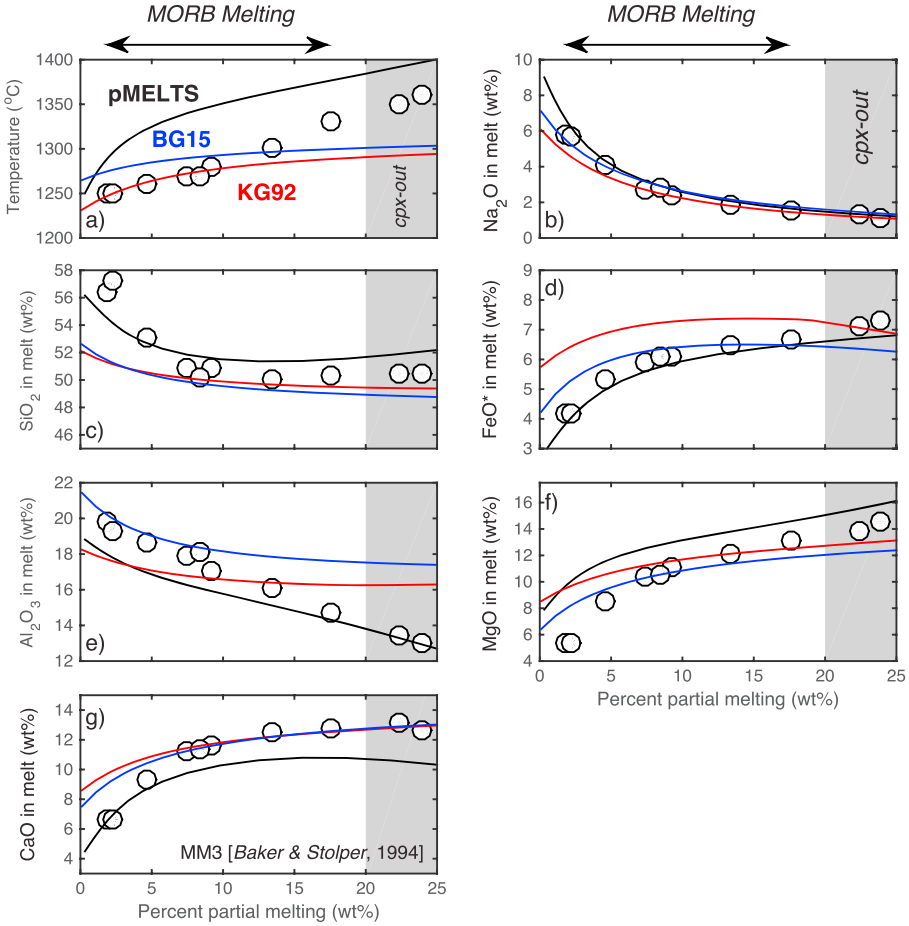

Figure 2. Comparison of melting models (solid lines) to experimental data on peridotite melting at 10 kbar (open circles) [*Baker and Stolper*, 1994; *Baker et al*., 1995]. (a) Melting temperature and (b) Na_2O, (c) SiO_2, (d) FeO, (e) Al_2O_3, (f) MgO, and (g) CaO in the melt as a function of melt fraction. Calculations are shown for models BG15 (blue), KG92 (red), and pMELTS (black). All calculations assume isobaric batch melting and the primitive upper mantle composition MM3 used in the experiments. No *f*O2 buffer was used in the pMELTS calculations.

modeling because it allows us to compare the calculated melt compositions to MORB data sets corrected to the same MgO content. In all calculations the pressure of crystallization is tied to the depth at which melting is terminated based on our thermal model [e.g., *Shaw et al*., 2010].

3. Results

3.1. Comparison to Laboratory Data and Other Melting Models

Before applying our new model to specific ridge settings, we compared the temperature and melt compositions calculated from our melting model to experimental data on peridotite melting. For isobaric batch melting of a primitive upper mantle composition (MM3) [*Baker and Stolper*, 1994; *Baker et al*., 1995] at 10 kbar, BG15 provides good fits to the Na_2O, FeO*, CaO, and MgO content of the experimental melts over the range of melt fractions expected beneath MORs ($F = 0$–20%), with slight errors in SiO_2 and Al_2O_3 at low and high melt fractions, respectively (Figure 2). The misfits at high melt fractions (>20%) are expected, because BG15 cannot be used to predict melt compositions when clinopyroxene is exhausted from the residue. BG15 also predicts similar melting temperatures to those observed in the laboratory, though with a slightly lower slope than in the experimental data. For comparison, pMELTS also fits the experimental data on MM3 well; however, it predicts systematically higher melting temperatures (by ~50°C) for a given melt fraction. To further test the BG15 melting parameterization, we compared the calculated melt compositions to experimental data on melting of a fertile mantle peridotite over pressures

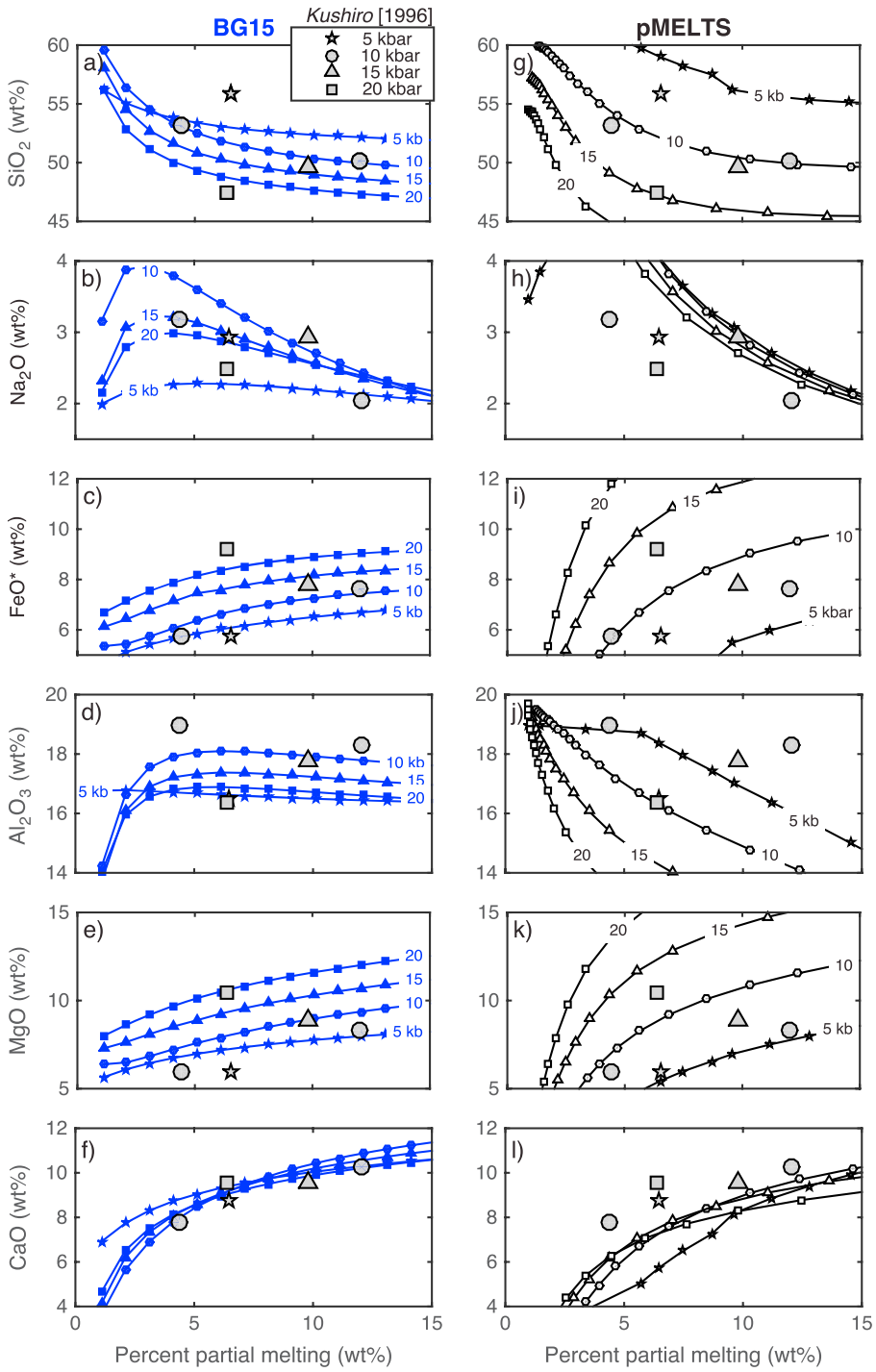

Figure 3. Comparison of (a–f, blue) BG15 and (g–l, black) pMELTS with the experimental data of *Kushiro* [1996] at a range of pressures from 5 to 20 kbar. (Figures 3a and 3g) SiO_2, (Figures 3b and 3h) Na_2O, (Figures 3c and 3i) FeO, (Figures 3d and 3j) Al_2O_3, (Figures 3e and 3k) MgO, and (Figures 3f and 3l) CaO in the melt as a function of melt fraction. Experiments at pressures of 10–20 kbar are saturated in spinel; the 5 kbar experiment is saturated in plagioclase. No *f*O2 buffer was used in the pMELTS calculations. Note that BG15 does a significantly better job at reproducing the experimental data over the entire pressure range than does pMELTS.

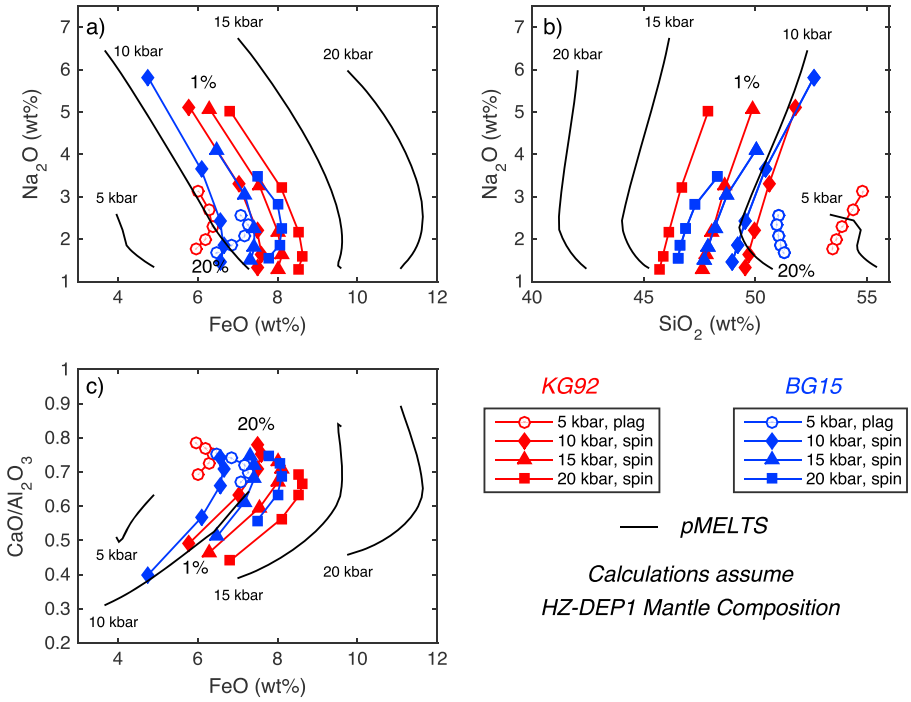

Figure 4. (a–c) Predicted melt composition for isobaric batch melting calculations at a range of pressures. Calculations are shown for melt increments of 1, 5, 10, 15, and 20% for models BG15 (blue) and KG92 (red). The symbols denote the pressure of melting. The 10–20 kbar calculations are performed in the spinel field (filled symbols); the 5 kbar calculations are performed in the plagioclase field (open circles). The pMELTS calculations are performed along a fayalite-magnetite-quartz (FMQ) *f*O2 buffer from 0.1 to 20% melting and shown in black in 0.1% increments. All calculations assume the *HZ-Dep1* mantle composition [*Kinzler and Grove*, 1992b]. Note that the composition of the initial 1% melts is highly pressure dependent for BG15 due to the incorporation of the pressure dependence of alkali partitioning between melt and pyroxene. This effect was ignored in KG92 and is not apparent in the predictions of pMELTS.

from 5 to 20 kbar [*Kushiro*, 1996]. Figures 3a–3f show that BG15 is able to predict the experimental melt compositions over the full pressure range (in both the spinel and plagioclase stability fields) up to melt fractions of ~12 wt %. By contrast, pMELTS does not reproduce *Kushiro*'s [1996] experimental compositions, displaying increasingly large misfits at higher pressures (Figures 3g–3l).

We also compared the predictions of BG15 to those of KG92 and pMELTS for isobaric batch melting of a depleted MORB mantle composition (*HZ-Dep1* in Table 1a of *Kinzler and Grove* [1992b]). As expected, BG15 predicts systematically higher FeO and lower SiO_2 in the melt at greater pressures (Figure 4). Moreover, within the spinel stability field there is a progressive increase in the Na_2O content of the lowest-degree melts with decreasing pressure. This is caused by the incorporation of the pressure-dependent partitioning of Na into pyroxene (Figure S1), which was not available for the KG92 model (compare 1% melts predicted by BG15 and KG92 in Figure 4a). The pressure dependence of the alkali partitioning in BG15 can also be seen in CaO/Al_2O_3 shown in Figure 4c. Also note that BG15 predicts melts within the plagioclase stability field to have FeO contents similar to the 10–15 kbar spinel melts. This is an important difference from KG92, which predicted that melts in the plagioclase field would be lower in FeO than melts in the spinel field, and results from the pressure dependence of the Fe-Mg K_Ds. The smaller input data set for KG92 did not cover a sufficient pressure range to reveal these systematics. Finally, compared to both BG15 or KG92, pMELTS predicts a much stronger pressure sensitivity in terms of the FeO and SiO_2 contents of the melt and predicts low-degree melts with very high Na_2O (≥6 wt %) at pressures ≥15 kbar.

3.2. Melting Along a 1-D Mantle Adiabat

We next investigated incremental batch melting along several 1-D mantle adiabats (Figure 5). As described above, we examine two different end-member parameterizations for melt productivity: (1) constant $dF/dP = 1\%\ \text{kbar}^{-1}$ and (2) variable dF/dP as a function of pressure (Figure 5b). In the latter case, we assume a linear increase in

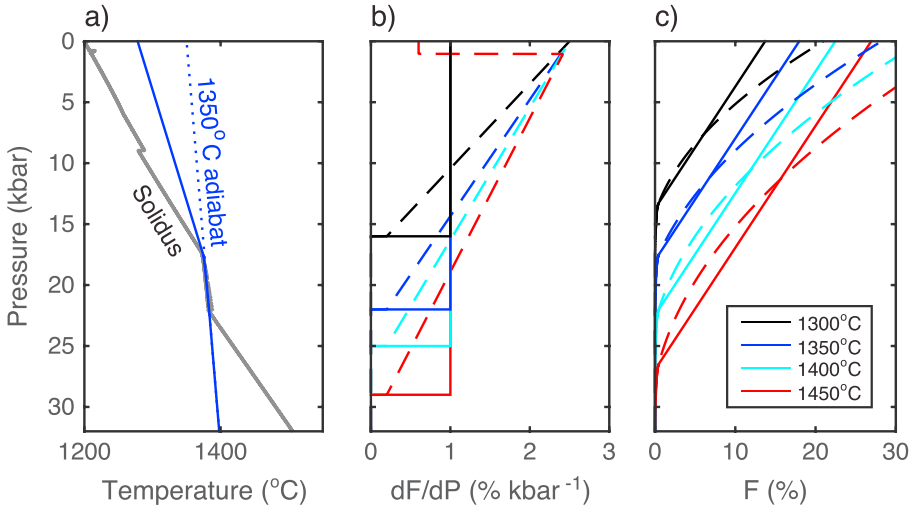

Figure 5. (a) Sample calculation of melting along a 1350°C mantle adiabat (dotted line). Calculation shown in Figure 5a assumes a constant melt productivity of 1% kbar^{-1} and an adiabatic gradient of 1.5°C kbar^{-1}. The solid blue line indicates the temperature after incorporation of latent heat of melting; the solid gray line denotes the mantle solidus as it evolves with pressure and mantle composition. (b) Parameterization of melt productivity as a function of mantle temperature: constant dF/dP = 1% kbar^{-1} (solid lines) and variable dF/dP as a function of pressure (dashed). Note that after cpx-out melt productivity is assumed to drop to 0.5% kbar^{-1}. (c) Calculated melt fraction (F) as a function of pressure for different mantle temperatures and melt productivities shown in Figure 5b.

dF/dP from 0.1% kbar^{-1} where the adiabat crosses the solidus to 2.5% kbar^{-1} at the surface. This is meant to represent a simplified parameterization for the variations in melt productivity predicted in thermodynamic calculations of isentropic melting [*Asimow et al.*, 1997, 2001]. For constant dF/dP, the degree of melting increases linearly to a maximum melt fraction (F_{max}) of 12% and 26% for mantle potential temperatures of 1300°C and 1450°C, respectively; F_{max} is approximately 50% greater for cases with variable dF/dP (Figure 5c). In these 1-D calculations no lithospheric lid is imposed and melting is assumed to continue to the surface as the mantle upwells at a constant rate. However, an important aspect of these end-member melt productivity functions is that for a 1350°C adiabat and a lithospheric lid thickness of 3–4 kbar (appropriate for a spreading rate of ~2 cm/yr [*Montési and Behn*, 2007]), the variable dF/dP end-member results in an average melt productivity over the entire melting region of ~1% kbar^{-1}, roughly equivalent to the constant dF/dP end-member.

We find that only in the cases with variable dF/dP and a mantle potential temperature ≥1450°C is clinopyroxene exhausted in the mantle residue for *Workman and Hart*'s [2005] depleted MORB mantle (DMM) composition (Figure 6). This is a result of the strong temperature dependence of Ca partitioning in clinopyroxene [*Till et al.*, 2012], which leads to an increase in the modal abundance of clinopyroxene at the high pressures and temperatures where melting occurs. For most ridge environments cpx-out does not limit mantle melting, and the decrease in modal clinopyroxene in abyssal peridotite residues is a consequence of subsolidus cooling and reequilibration after melting has ceased. It is not evidence for the exhaustion clinopyroxene during melting.

An interesting feature of our calculations is that even when a constant dF/dP is imposed, there is an interval at the base of melting regime where the depth-averaged melt productivity is quite low (~0.1% kbar^{-1}). In this region, the solidus temperature is highly sensitive to small amounts of depletion associated with the removal of K_2O from the mantle residue [*Till et al.*, 2012]. The result is that the first K_2O-rich melt increments raise the solidus temperature and result in a region where the solidus and the adiabat are approximately collinear (e.g., between 22 and 16 kbar for a 1350°C adiabat; Figure 5a). Eventually, K_2O is sufficiently depleted from the residue that the solidus becomes more strongly controlled by the other compositional variables (1-Mg#, TiO_2, and NaK#) and melt production is governed primarily by the imposed dF/dP.

The composition of incremental batch melts (assuming 90% melt removal at each step) and the pooled melts for the entire melting column were calculated for both parameterizations of melt productivity and mantle

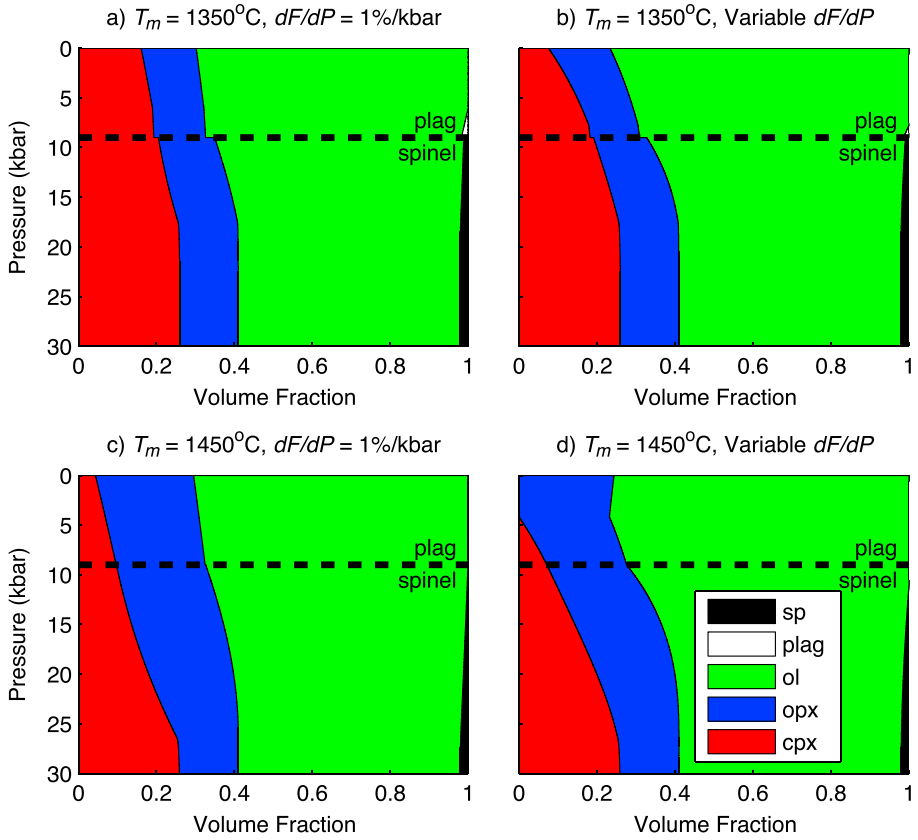

Figure 6. Calculated high-pressure mantle melting mode from BG15 as a function of mantle potential temperature (T_m) and melt productivity (dF/dP). (a) $T_m = 1350$°C, constant $dF/dP = 1\%\ \text{kbar}^{-1}$. (b) $T_m = 1350$°C, pressure-dependent dF/dP. (c) $T_m = 1450$°C, constant $dF/dP = 1\%\ \text{kbar}^{-1}$. (d) $T_m = 1450$°C, pressure-dependent dF/dP. Calculations assume the DMM composition of *Workman and Hart* [2005]. Note that only in case with a 1450°C mantle and pressure-dependent melt productivity is cpx exhausted from the mantle residue, suggesting that cpx-out does not terminate melting beneath most mid-ocean ridges.

temperatures of 1350°C and 1450°C (Figures 7 and 8). For constant $dF/dP = 1\%\ \text{kbar}^{-1}$, BG15 predicts pooled melt compositions that are slightly lower in FeO, but similar in Na_2O and SiO_2, compared to KG92 (compare large symbols in Figure 7). Note that there is a jump in the incremental melt compositions when melting crosses the spinel-plagioclase transition imposed at 0.9 GPa. This jump is most pronounced along the cooler 1350°C adiabat (open symbols), where less total melting has occurred and the incremental melts remain more enriched when they enter the plagioclase field.

For cases with a variable dF/dP, we compared the pressure-dependent dF/dP calculations from BG15 to isentropic predictions from pMELTS (Figure 8). For the same range in mantle potential temperature there is a larger variation in the FeO and SiO_2 contents of the pooled melts as predicted by pMELTS compared to BG15. Specifically, pMELTS predicts pooled melts with lower FeO compared to BG15 along the 1350°C geotherm but higher FeO along the 1450°C geotherm (Figure 8a). The pMELTS also predicts a much wider range in incremental melt compositions, consistent with the isobaric fractional melting calculations shown in Figure 4. An implication of this comparison is that when these melting models are used to interpret observed MORB glass chemistry, a larger variation in mantle potential temperature will be inferred when comparing data with different FeO contents based on BG15 compared to interpretations made using pMELTS. Finally, we note that the melt fraction and temperature profiles calculated using BG15 with variable dF/dP are reasonably similar to those predicted by pMELTS (Figures 8c and 8d), supporting our use of this as an end-member productivity function.

3.3. Two-Dimensional Melting Beneath a Mid-Ocean Ridge

Using the BG15 melting model, we next investigate predictions of crustal thickness and primary MORB chemistry for a 2-D mid-ocean ridge as a function of mantle potential temperature and spreading rate

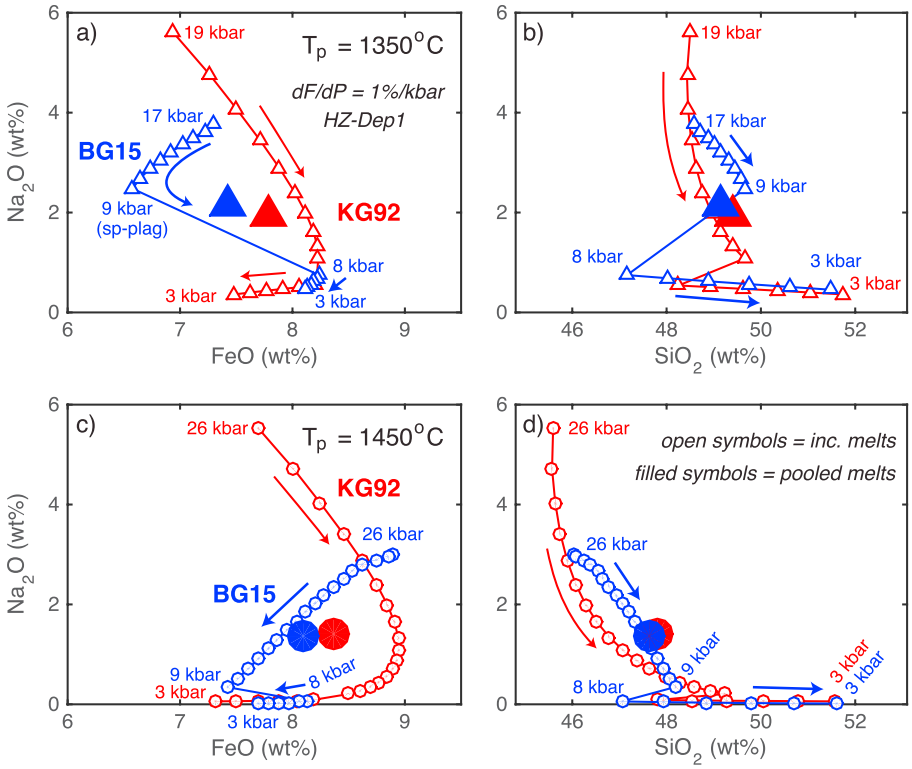

Figure 7. Predicted melt compositions calculated assuming incremental batch melting with 90% extraction at each step along a (a and b) 1350°C and (c and d) 1450°C adiabat, respectively. Calculations assume a constant $dF/dP = 1\%\ \text{kbar}^{-1}$ and an adiabatic gradient of $1.5°\text{C kbar}^{-1}$. Results are shown for models BG15 (blue) and KG92 (red). The small open symbols denote the incremental melts in 1% increments; the large filled symbols show the pooled melts. The arrows illustrate the progression of melting with pressure steps denoted. Note the large discontinuity in melt compositions (particularly FeO) predicted by BG15 across the spinel-plagioclase phase transition. Calculations assume the *HZ-Dep1* mantle composition [*Kinzler and Grove*, 1992b].

(Figure 9). For each scenario, the calculated thermal structure and mantle flow field are used to predict melt production rate and incremental melt chemistry throughout the model domain (e.g., Figure 1). An important difference between these calculations and the simpler 1-D models shown in Figures 7 and 8 is the presence of a thermal lid and variable upwelling rates, which are calculated in a self-consistent manner from the 2-D geodynamic models. We investigate the following melting parameters: *dF/dP*, initial mantle depletion, and the horizontal length scale over which melts are pooled to the ridge axis.

Given the number of factors influencing melting, we simplify the following discussion by first defining a base case with constant $dF/dP = 1\%\ \text{kbar}^{-1}$, the DMM composition of *Workman and Hart* [2005] for the initial mantle, and full pooling of all melts across the model domain. The results of the base case are denoted by solid lines in Figures 9a–9d. For these parameters, we find that mantle potential temperature has the greatest influence on crustal thickness and melt chemistry, while spreading rate influences melting at the slowest rates, where it produces systematically lower crustal thickness and higher Na_2O contents in the melt. An important result of these calculations is that while crustal thickness inferred from numerical models with constant mantle viscosity (i.e., purely passive flow) typically increases monotonically with spreading rate [*Sotin and Parmentier*, 1989; *Braun et al*., 2000], for a given mantle potential temperature, our calculated crustal thickness estimates plateau at half rates >3 cm/yr. This behavior is more typical of models that incorporate buoyancy [e.g., *Sotin and Parmentier*, 1989; *Braun et al*., 2000; *Katz*, 2010] in which the relative contribution of buoyancy-induced upwelling (compared to passive upwelling) is greater at slower spreading rates. Although our models do not incorporate buoyancy, the visco-plastic rheology we employ results in a similar effect. Specifically, plastic failure preferentially thins the axial lithosphere relative to the lithosphere off axis. This results in upwelling rates that exceed the analytical value for isoviscous

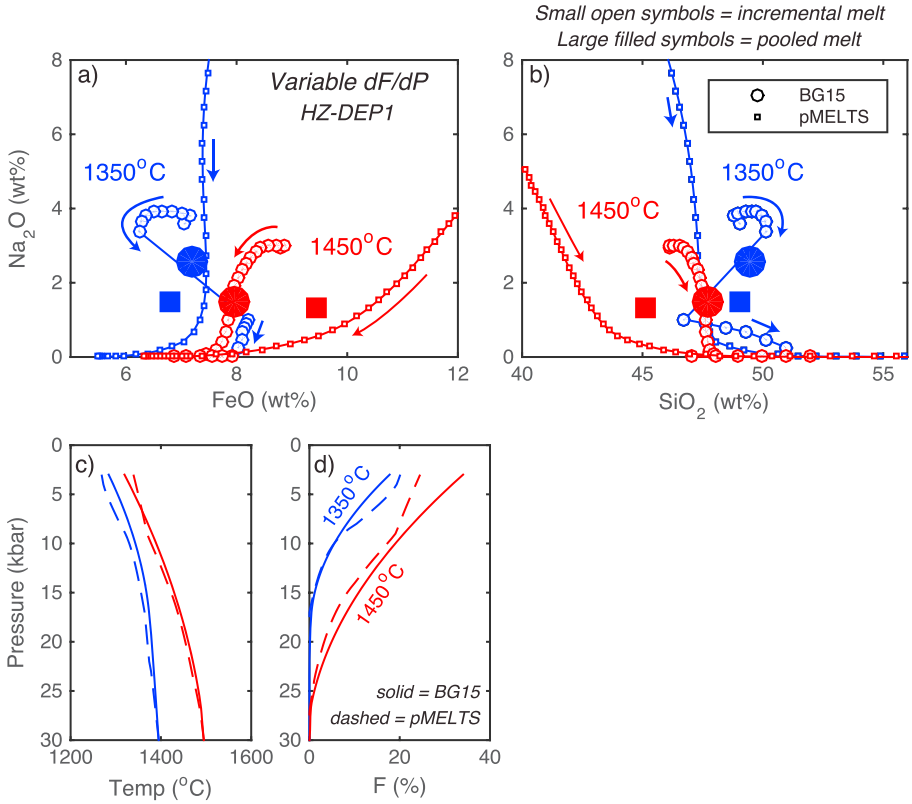

Figure 8. (a and b) Comparison of predicted melt compositions from BG15 with pressure-dependent *dF/dP* (circles) and pMELTS (squares). Calculations assume incremental batch melting with 90% extraction at each step along a 1350°C (blue) and 1450°C (red) adiabat. The pMELTS calculations were performed along an FMQ *f*O2 buffer. The small open symbols denote the incremental melts; the large filled symbols the show pooled melts. All calculations use the *HZ-Dep1* mantle composition [*Kinzler and Grove*, 1992b]. Note that a melting increment of 1% is used in the calculations with BG15 but is dynamically set based on an imposed pressure step of 0.5 kbar in pMELTS. (c) Temperature and (d) melt fraction *F* as a function of pressure as calculated from BG15 (solid lines) and pMELTS (dashed lines).

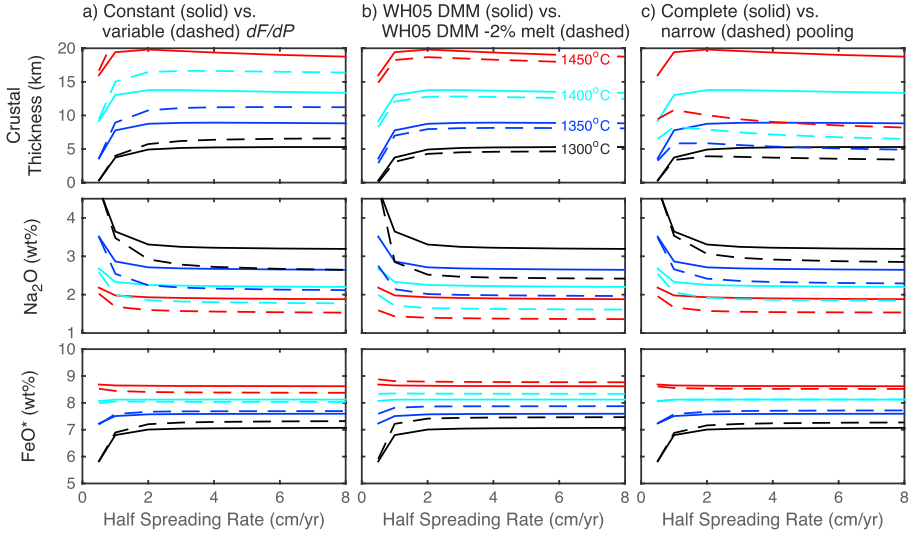

Figure 9. Effects of (a) constant versus pressure-dependent *dF/dP*, (b) DMM versus depleted DMM composition, and (c) complete versus narrow pooling on crustal thickness and Na_2O and FeO in pooled primary melts as a function of half spreading rate. The colors correspond to the different mantle potential temperatures (black = 1300°C; dark blue = 1350°C; light blue = 1400°C; red = 1450°C). The solid lines are the same in Figures 9a–9c and correspond to the reference case with complete pooling, constant $dF/dP = 1\%\ \text{kbar}^{-1}$, and the *Workman and Hart*'s [2005] DMM mantle composition.

corner flow ($\pi/2$ times half spreading rate [*Batchelor*, 1967]), focuses upwelling beneath the ridge axis, and produces more crust relative to isoviscous calculations. This effect is most pronounced at slow to ultraslow-spreading rates, where the lithosphere is thickest and plastic failure results in greater lithospheric thinning compared to faster spreading environments.

We next investigate the effects of melt productivity, mantle depletion, and pooling geometry relative to the base case (Figure 9). Figure 9a illustrates the effect of variable *dF*/*dP* on crustal thickness and melt chemistry. Overall, variable *dF*/*dP* produces greater total degrees of melting (Figure 5c) and thus results in thicker crust and lower Na_2O concentrations compared to the base case (Figure 9a). FeO is only slightly affected by the melt productivity, with variable *dF*/*dP* leading to smaller variations in FeO as a function of mantle temperature compared to the constant *dF*/*dP* case. To assess the influence of mantle depletion, we examined a case in which we first extracted 2% melt from *Workman and Hart*'s [2005] DMM composition (using BG15) and then used this depleted composition as our starting mantle composition (Figure 9b). Relative to the base case, this results in slightly thinner crust (due to the elevated solidus of the depleted mantle), a large decrease Na_2O (due the prior extraction of the more incompatible elements), and slightly elevated FeO.

Finally, we examined the importance of melt pooling using a series of cases in which all melts produced >25 km off axis were excluded from the aggregate melt compositions and do not contribute to the calculated crustal thickness (Figure 9c). Reducing the contribution of the off-axis (or "wing") melts decreases crustal thickness, with the largest effects at high mantle potential temperatures and fast spreading rates. For example, for a mantle potential temperature of 1350°C, limiting the pooling width will decrease crustal thickness by 25% and 40% for half spreading rates of 1 and 8 cm/yr, respectively. Similarly, melt chemistry is most strongly affected at faster spreading rates, with systematically lower Na_2O contents for the narrow pooling region (due to the decreased contribution of the lower degree, more enriched off-axis melts). The effect of melt pooling on FeO content is modest and dependent on the mantle potential temperature. The reason for the more pronounced differences compared to the base case at high mantle temperatures and faster spreading rates is that these regimes produce significantly more off-axis melt, which for the narrow pooling cases is assumed to be lost due to refreezing in the overlying lithosphere.

In summary, all three scenarios (variable *dF*/*dP*, initial mantle depletion, and narrow melt pooling) result in decreased Na_2O content of the melts relative to the base case. However, changing these parameters results in systematically different predictions of crustal thickness and FeO content—thus motivating an examination of whether these effects can be isolated and better constrained in joint analyses of global MORB chemistry and seismically determined crustal thickness data.

4. Discussion

BG15 represents a substantial improvement over previous thermodynamically based melting models for calculating MORB chemistry as a function of mantle melting parameters. While not as flexible in terms of the range of compositional and thermodynamic variables that can be explored with pMELTS, BG15 is more accurately tuned for investigating melting in mid-ocean ridge environments. Moreover, its computational simplicity allows it to be easily incorporated into geodynamic models as illustrated above. Below we turn our attention to using the predictions of BG15 to evaluate the parameters that control melt generation beneath the global mid-ocean ridge system.

4.1. Observed Variability in MORB Chemistry and Crustal Thickness

Global variations in mid-ocean ridge melting have been inferred based on joint observations of MORB chemistry, axial ridge depth, and when available seismically determined crustal thickness [e.g., *Klein and Langmuir*, 1987]. Ridges with shallower axial bathymetry are typically characterized by lower Na_8 and higher Fe_8, indicating a longer melting column and greater crustal production [e.g., *Klein and Langmuir*, 1987; *Langmuir et al*., 1992]. In this interpretation, axial bathymetry is used as a proxy for crustal thickness assuming local isostatic equilibrium [*Klein and Langmuir*, 1987]. While this interpretation is likely robust to first order, a weakness of this approach is that axial lithosphere supports significant flexural stresses [*Neumann and Forsyth*, 1993; *Escartín and Lin*, 1998], and thus, it is difficult to accurately infer crustal production directly from axial bathymetry.

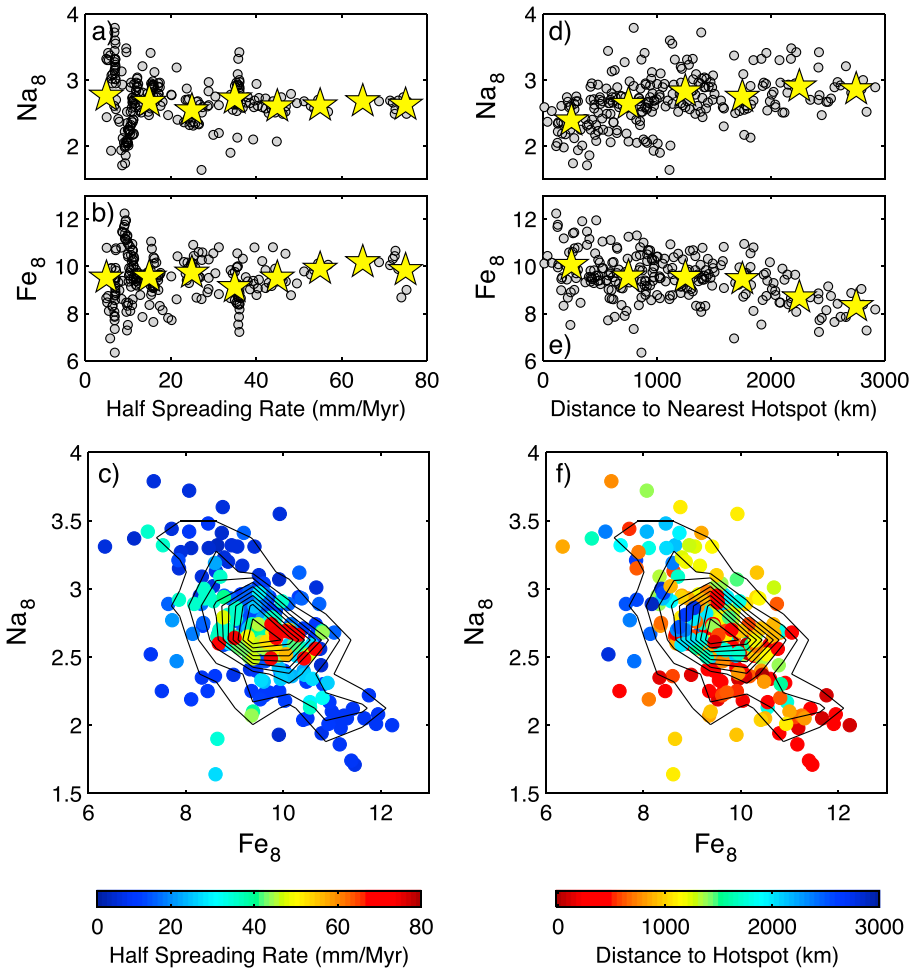

Figure 10. Segment-averaged Na_8 and Fe_8 from global MORB compilation of *Gale et al.* [2014] as a function of (a–c) spreading half rate and (d–f) distance to the nearest hot spot. The small gray circles in Figures 10a, 10b, 10d, and 10e are the individual segment averages; the yellow stars are the averages binned in half rate increments of 10 mm/yr in Figures 10a and 10b and averages binned in 500 km distance increments in Figures 10d and 10e. The contours in Figures 10c and 10f illustrate the concentration of the data points. Note that there is a strong global correlation between MORB chemistry and distance to the nearest hot spot but a much weaker correlation with spreading rate.

A more direct measure of melt production is seismically determined crustal thickness. However, in comparison to axial bathymetry, which can easily be determined globally, seismic refraction studies offer relatively sparse coverage over the global ridge system. For example, at the time of *Klein and Langmuir*'s [1987] seminal study, only seven data points existed for "normal" ridge segments not affected by hot spots. However, data collected over the last 20–30 years have increased this data set fourfold and now provide reasonably complete sampling over the global range of mid-ocean ridge spreading rates.

To investigate the parameters that control melt generation beneath the global mid-ocean ridge system, we compare predictions of the BG15 model to observations of MORB chemistry and co-located seismic determinations of crustal thickness. We evaluate MORB chemistry using the recent compilation of fractionation-corrected major element data from *Gale et al.* [2014]. This compilation includes segment-averaged compositions for 241 individual spreading segments that span the global range in mid-ocean ridge spreading rates (Figure 10). Crustal thickness data were compiled from all available on-axis seismic experiments, starting with the compilation of *White et al.* [2001] and supplemented with additional data sets [*Tolstoy et al.*, 1993; *Navin et al.*, 1998; *Hooft et al.*, 2000; *Canales et al.*, 2002, 2000; *Detrick et al.*, 2002; *Canales et al.*, 2003; *Ljones et al.*, 2004; *Carbotte et al.*, 2008; *Seher et al.*, 2010; *Jokat et al.*, 2012]. We focused on seismic data sets located on active spreading centers, as co-located geochemical information is not typically available for

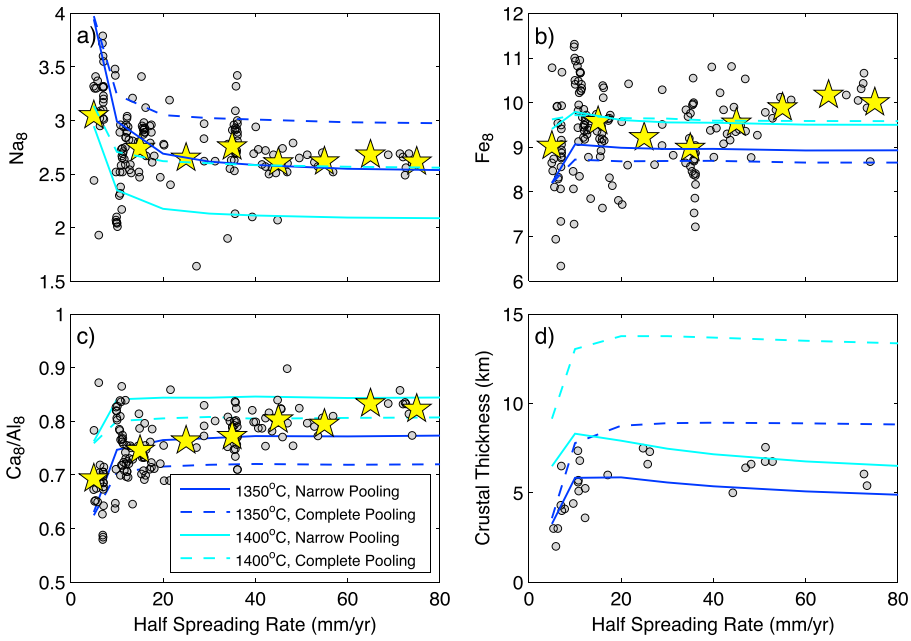

Figure 11. Comparison of BG15 model predictions assuming a constant $dF/dP = 1\%\ \text{kbar}^{-1}$ to segment-averaged MORB compositions and seismically determined crustal thickness. (a) Na_8, (b) Fe_8, and (c) Ca8/Al8 in the pooled melt and (d) crustal thickness calculated as a function of spreading half rate. The small gray circles in Figures 11a–11c are the individual segment averages from global MORB compilation of *Gale et al.* [2014] for segments >750 km from the nearest hot spot; the yellow stars are the averages of these data binned in 10 mm/yr increments. The small gray circles in Figure 11d are the subset of segments for which seismically determined crustal thickness estimates are available. The dark and light blue lines correspond to the calculations along 1350° and 1400°C mantle adiabats, respectively. The dashed lines denote the complete melt pooling; the solid lines show the narrow pooling of melts within 25 km of the ridge axis. All calculations assume the *Workman and Hart*'s [2005] DMM mantle composition. Note that only the case with a mantle potential temperature of 1350°C and narrow pooling (solid dark blue line) fits both the MORB compositions and the crustal thickness data.

off-axis regions. We note that this results in a more limited data set (27 ridge segments) compared to the full compilation of *White et al.* [2001]; however, the first-order crustal thickness constraints remain the same, namely, (1) the oceanic crust has an average thickness of 6–7 km for half rates >1–2 cm/yr and (2) oceanic crust is thinner and more variable in thickness at half rates ≤1 cm/yr (Figure 11d).

4.2. Na_8-Fe_8 Systematics

It has long been recognized that mantle temperature plays a first-order role in controlling MORB chemistry [e.g., *Klein and Langmuir*, 1987; *McKenzie and Bickle*, 1988; *Niu and Batiza*, 1991; *Kinzler and Grove*, 1992b; *Langmuir et al.*, 1992]. To illustrate this effect, we plot *Gale et al.*'s [2014] segment-averaged Na_8 and Fe_8 values relative to distance to the nearest hot spot (Figures 10d–10f). Compared to spreading rate, which shows little correlation with Na_8 and Fe_8 for all 241 segments (Figures 10a–10c), robust correlations are found between Na_8 and Fe_8 and distance to the nearest hot spot—with ridges near hot spots characterized by lower Na_8 and higher Fe_8. Assuming that hot spots are indicative of a warmer ambient mantle [e.g., *Morgan*, 1971, 1972; review by *Ito and van Keken*, 2007], this correlation is consistent with a longer melting column and greater degree of melting beneath ridge segments adjacent to hot spots [*Klein and Langmuir*, 1987; *Langmuir et al.*, 1992].

To estimate the range in mantle temperature required to explain the global MORB data set, *Gale et al.* [2014] used pMELTS and the empirical melting model of *Langmuir et al.* [1992] (hereafter referred to as LKP92) to predict pooled melt compositions as a function of mantle temperature (Figure 12). Calculations from pMELTS are consistent with a global variation in mantle potential temperature of 1350–1450°C; however, the pMELTS calculations (shown by light blue circles in Figure 12) do not reproduce the slope of the first-order trend observed in the global Na_8-Fe_8 data set. Specifically, pMELTS significantly underpredicts the magnitude of the global variability in Na_8 relative to Fe_8. This result is consistent with previous studies,

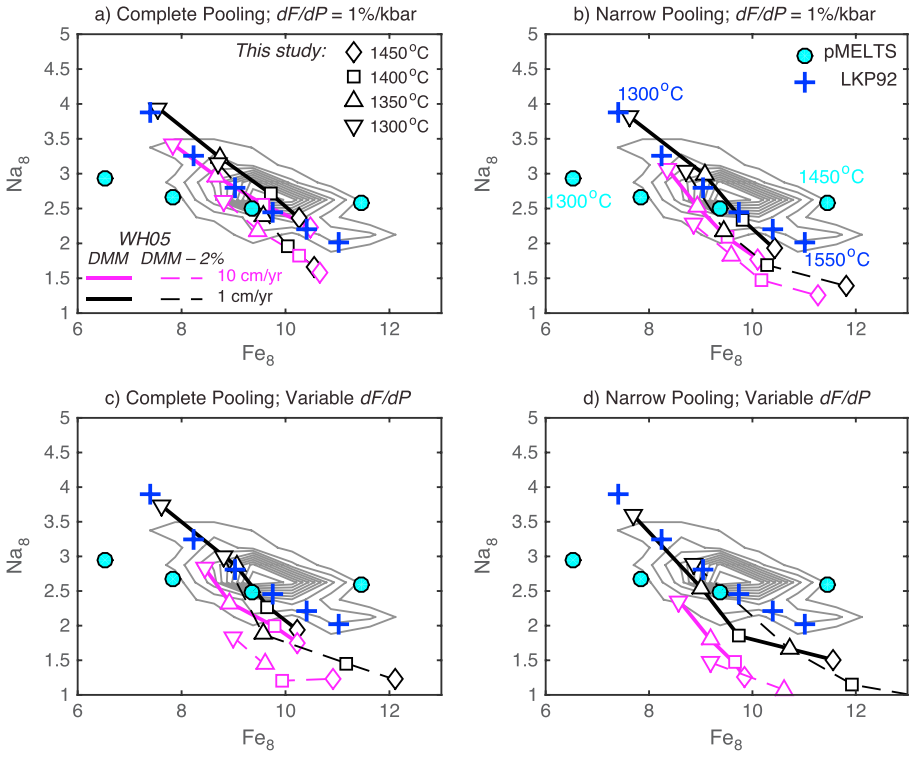

Figure 12. Na_8 versus Fe_8 in the pooled melt calculated from BG15 assuming complete and narrow pooling for (a and b) constant $dF/dP = 1\%\ kbar^{-1}$ and (c and d) pressure-dependent dF/dP. The solid lines correspond to the WH05 DMM; the dashed lines correspond to the WH05 DMM–2% melt. The magenta and black lines denote the half spreading rates of 10 and 1 cm/yr, respectively. The open symbols show the BG15 calculations for different mantle potential temperature (inverted triangle = 1300°C; triangle = 1350°C; square = 1400°C; diamond = 1450°C). The light blue filled circles and blue crosses correspond to the calculations at 50°C temperature increments using pMELTS and LKP92, respectively, from *Gale et al.* [2014]. The contours denote the data density from the global MORB database of *Gale et al.* [2014] as shown in Figure 9. BG15 makes very similar predictions to LKP92 assuming narrow pooling and constant $dF/dP = 1\%\ kbar^{-1}$ (Figures 12a and 12b). Both models provide a good fit to the overall trend in the global MORB database, although BG15 requires a smaller temperature range than does LKP92. The pMELTS underpredicts the global variability in Na_8 relative to Fe_8.

which have found it difficult to accurately predict experimental data and MORB chemistry from pMELTS [e.g., *Robinson et al.*, 1998; *Hirschmann et al.*, 1998; *Gaetani*, 1998; *Langmuir et al.*, 2006]. By contrast, *Gale et al.* [2014] found that LKP92 (blue crosses in Figure 12) better predicts the slope of the global Na_8-Fe_8 data set but requires a wider range in mantle temperature (~1300–1550°C as compared to ~1350–1450°C for pMELTS; see Figure 20 of *Gale et al.* [2014]) to fit the data. This wider range was also found to be consistent with temperature anomalies inferred from the magnitude of seismic shear wave velocity anomalies beneath mid-ocean ridges [*Dalton et al.*, 2014], although when ridge segments >700 km from a hot spot are excluded from their analysis, *Dalton et al.* [2014] found that the remaining segments were best fit with a narrower temperature range of 1300–1450°C.

Here we use BG15 to reassess the range in mantle potential temperature required to fit the global Na_8-Fe_8 data set. For direct comparison with the *Gale et al.*'s [2014] segment-averaged data, we first correct the calculated primary melt compositions shown in Figure 9 to 8 wt % MgO using the fractional crystallization model of *Yang et al.* [1996] and assuming a crystallization pressure corresponding to the top of the melting regime [*Gregg et al.*, 2009]. Overall, *Gale et al.*'s [2014] data set is well fit by either complete or narrow pooling at a constant $dF/dP = 1\%\ kbar^{-1}$; poorer fits are obtained with models that incorporate variable dF/dP, which tend to underpredict Na_8 at $Fe_8 > \sim 9$ (Figures 9c and 9d). For constant dF/dP, BG15 produces a similarly good fit to the slope of the global Na_8-Fe_8 data set as does LKP92 and predicts a comparable variation in mantle potential temperature from ~1325 to 1450°C (Figure 12).

Thus, in summary, our coupled petrologic-geodynamic calculations show that for a constant $dF/dP = 1\%\,\text{kbar}^{-1}$ and a DMM mantle source, the predicted trends in Na_8-Fe_8 fit the global data set reasonably well regardless of melt pooling geometry (Figures 12a and 12b). By contrast, calculations with a variable dF/dP tend to underpredict Na_8 for a given Fe_8 (Figures 12c and 12d). This indicates that the calculations with variable dF/dP produce too high a degree of melting near the top of the melting column, particularly for hotter mantle geotherms. A possible explanation for this is that our pressure-dependent melt productivity function overpredicts dF/dP at low pressure. Similarly, depletion of the mantle source (e.g., DMM–2% melt) tends to move the pooled melt compositions toward lower Na_8 for a given Fe_8 (Figure 12), while more enriched compositions increase Na_8 relative to Fe_8. This result is similar to that found by *Gale et al.* [2014] and provides strong evidence that the first-order trend in the global Na_8-Fe_8 systematics is governed by mantle temperature variations as opposed to compositional differences. Finally, our calculations show that narrow versus full pooling has a relatively modest effect on pooled melt compositions compared to mantle temperature, but limiting the pooling width tends to shift the pooled melts toward slightly higher Fe_8 and lower Na_8, particularly at higher mantle potential temperatures (e.g., compare Figures 9a and 9b).

4.3. Constraints on Melt Pooling From Joint Analysis of MORB Chemistry and Crustal Thickness

While mantle temperature variations clearly represent the dominant signal in the global MORB data set, crustal thickness provides an additional constraint that can help isolate the effects of the melt pooling geometry beneath the ridge axis. The reason for this is twofold. First, limiting the pooling width has a strong influence on crustal thickness, which becomes more pronounced at higher mantle temperatures when there is significant off-axis melt production (Figure 9c). Second, as discussed above, limiting the pooling width results in a corresponding decrease in incompatible elements such as Na, because the melts excluded from the off-axis wings of the melt region are typically lower melt fraction and thereby more enriched. Thus, the covariability associated with jointly constraining both crustal thickness and MORB chemistry provides additional constraints compared to using either the chemical or crustal thickness data sets in isolation.

To illustrate this, we compare calculations of crustal thickness based on the BG15 model to an expanded set of fractionation-corrected oxide data from *Gale et al.* [2014] and our new compilation of seismically determined crustal thicknesses (Figures 13 and 14). Specifically, we show that while the base case (full melt pooling, constant $dF/dP = 1\%\,\text{kbar}^{-1}$, and DMM mantle source) reproduces the global trend in Na_8-Fe_8 (Figure 12a), it systematically overpredicts crustal thickness relative to Na_8, Fe_8, Si_8, Ca_8/Al_8, and K_8/Ti_8 (Figures 13a–13e). One way to improve the fit to the observed major element trends relative to crustal thickness is to use a depleted mantle source (e.g., DMM–2%); however, as shown in Figure 12a, this degrades the fit to the Na_8-Fe_8 data, particularly at high FeO. Thus, we prefer a model in which the pooling width is decreased to $\leq$25 km from the ridge axis, which simultaneously reproduces the global patterns in major element oxides and seismically determined crustal thickness for a DMM mantle source (solid lines in Figures 13f–13j). Assuming this narrow pooling regime, we find that all segments located $>$750 km from a hot spot (circles) can be explained by a variation in mantle temperature of 1300–1450°C, consistent with that inferred from upper mantle seismic shear wave anomalies at segments far from hot spots [*Dalton et al.*, 2014]. We note that the temperature range required to fit both the crustal thickness and geochemical data extends to slightly lower temperatures than if only Na_8-Fe_8 are considered (Figure 12b). Similar to the results for the global Na_8-Fe_8 systematics (Figures 12c and 12d), calculations assuming variable dF/dP do a poorer job at fitting the joint seismic and major element data set (Figure 14) than do those for a constant dF/dP of $1\%\,\text{kbar}^{-1}$ (Figure 13). In particular, at faster spreading rates ($>$5 cm/yr), the variable dF/dP model predictions tend to fall outside the global array, except for mantle temperatures of 1300–1350°C, and cannot reproduce observations at specific fast-spreading segments for Na_8, Fe_8, and Si_8 (compare magenta model curves with circles of the same color in Figures 14f–14h).

To further isolate the influence of pooling geometry from other melting parameters, we examined segments $>$750 km from a hot spot as function of spreading rate (Figure 11). While the global MORB data set shown in Figures 10a and 10b showed relatively little dependence on spreading rate, the more limited suite of spreading segments located far from hot spots shows a distinct lithospheric lid effect (decreased crustal thickness and elevated Na_8) at spreading rates below ~2 cm/yr half rate (Figure 11). Comparing these data with calculations from BG15, we find that Na_8, Fe_8, Ca_8/Al_8, and crustal thickness are best fit by a mantle

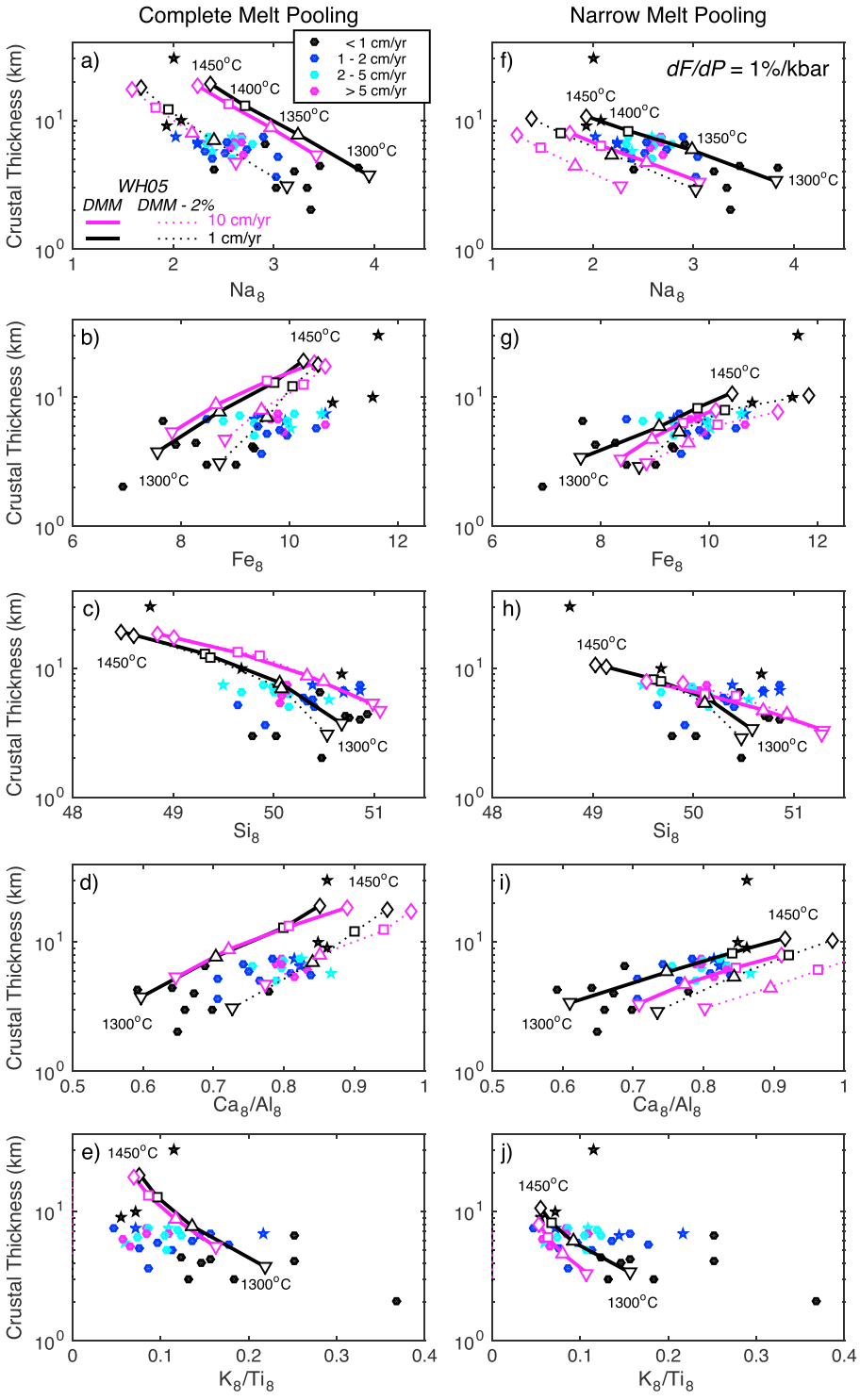

Figure 13. Fractionation corrected major element oxides Na_8, Fe_8, Si_8, Ca_8/Al_8, and K_8/Ti_8 in the pooled melt versus crustal thickness calculated from BG15 assuming a constant $dF/dP = 1\%\ kbar^{-1}$ for (a–e) complete and (f–j) narrow pooling. The solid lines correspond to the WH05 DMM; the dashed lines correspond to the WH05 DMM–2% melt. The magenta and black lines denote the half spreading rates of 10 and 1 cm/yr, respectively. The open symbols show calculations for different mantle potential temperatures (inverted triangle = 1300°C; triangle = 1350°C; square = 1400°C; diamond = 1450°C). The small filled symbols show the individual segment averages from *Gale et al.* [2014] and our data set of seismically determined crustal thickness color coded by spreading rate. The circles denote the segments >750 km from a hot spot; the stars denote the segments <750 km from a hot spot. Iceland is represented by the outlier with ~40 km crustal thickness. These calculations indicate that the MORB data are best fit by the WH05 DMM composition and narrow pooling within 25 km of the ridge axis.

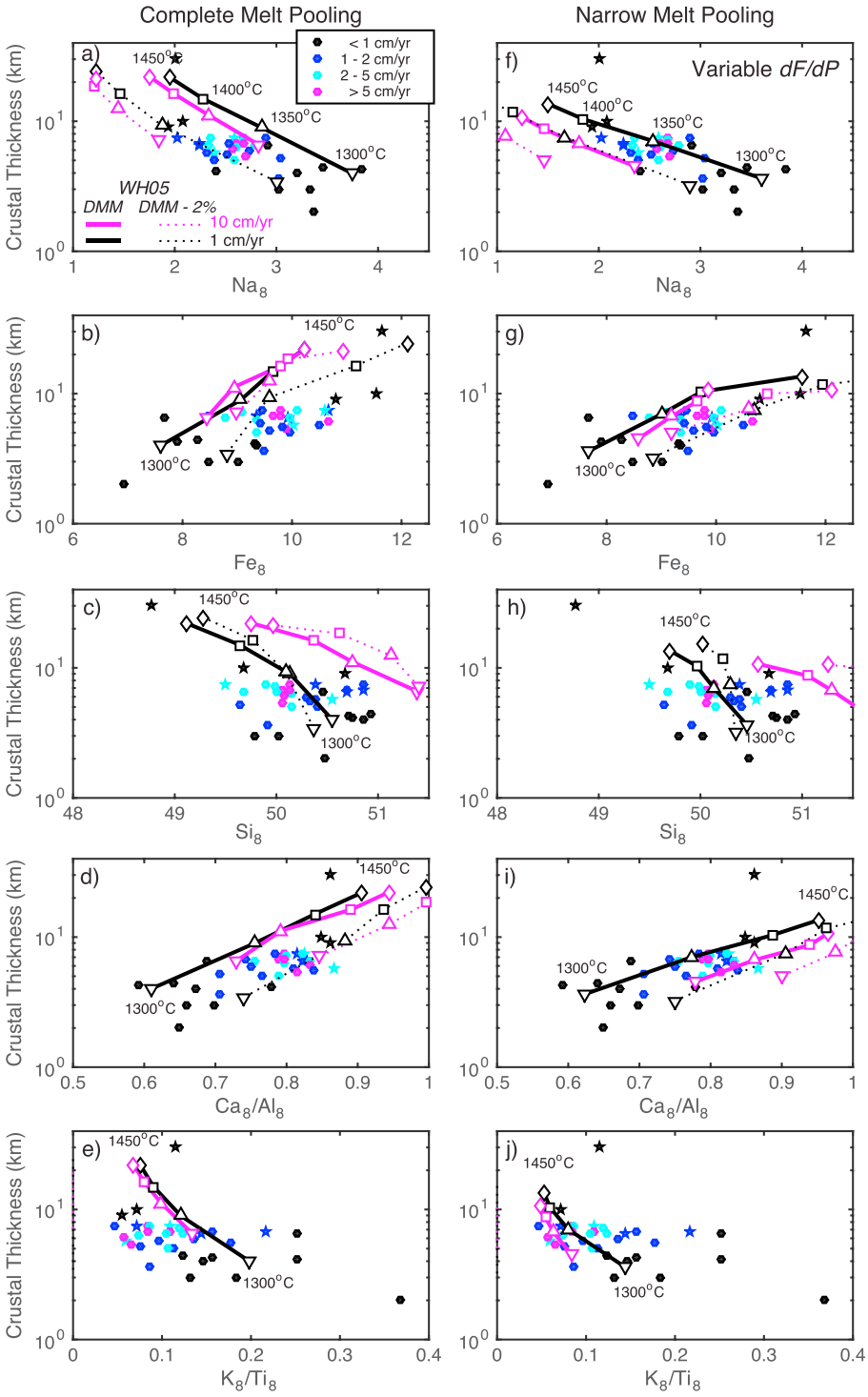

Figure 14. (a–j) Same as Figure 13 but calculated with variable *dF/dP*. Overall, the variable *dF/dP* results are a poorer fit to the global MORB and crustal thickness data sets.

potential temperature of 1350°C and a narrow zone of melt pooling isolated to ≤25 km from the ridge axis. We note that while a model with complete pooling and a mantle temperature of 1400°C can fit the available geochemical data (Figures 11a–11c), it produces crustal thicknesses that are considerably larger than observed (Figure 11d). This again illustrates the importance of combining geophysical and geochemical constraints in order to determine mantle melting parameters.

We hypothesize that the width of the pooling regime beneath the ridge axis is controlled by how efficiently ascending melts are transported laterally along the permeability barrier that forms at the base of the lithosphere [e.g., *Sparks and Parmentier*, 1991]. Assuming that the permeability barrier is generated by a crystallization front, then the strength of this barrier is related to the rate of crystallization, which is in turn controlled by the vertical temperature gradient [*Kelemen and Aharonov*, 1998; *Hebert and Montési*, 2010]. Moreover, the efficiency of buoyant melt transport along the permeability barrier is related to the slope of the barrier, with steeper slopes leading to more efficient transport of melt toward the ridge axis and shallower slopes resulting in refreezing of melt in the lithosphere [e.g., *Hebert and Montési*, 2010; *Montési et al*., 2011]. *Hebert and Montési* [2010] used calculations of crystallization rates for different spreading regimes to show that a strong permeability barrier, with a slope exceeding the critical slope for buoyant melt transport to the ridge axis, only extends 20–50 km off axis.

The length scale of melt pooling based our modeling of major element chemistry in MORBs is thus in accord with the calculations of *Hebert and Montési* [2010] and suggests that while MORB generation can extend upward of 100 km from the ridge axis, only those melts generated relatively close to the ridge axis contribute to the pooled MORB compositions erupted on axis. An important implication of this narrow pooling model is that ~20–40% of the total melt formed beneath the ridge does not contribute to the generation of the oceanic crust. Moreover, the melts that do refreeze in the lithosphere will be low-degree melts with relatively enriched compositions compared to the aggregate melts erupted on axis and thus may act as an important agent for lithospheric refertilization in global geochemical budgets. Future studies comparing crustal production and melt chemistry on a segment-by-segment basis are an important next step in order to determine how variable the width of pooling is across the global ridge system and whether pooling width exhibits a spreading rate dependence as predicted by *Hebert and Montési* [2010].

Finally, we note that even when limited pooling is incorporated in our models, there are still individual ridge segments that fall outside the bounds of our model predictions (Figure 13). This discrepancy is most pronounced for (1) Iceland, which has extremely high crustal thickness relative to its predicted Na_8 and Fe_8, and (2) several slow-spreading segments with thin crust but variable major element contents. We interpret this variability to reflect variations in mantle fertility, deeper melt contributions from garnet lherzolite, and/or more complicated 3-D patterns of melt pooling not considered here. For example, the slow-spreading segments with relatively thin crust that lie below the narrow pooling predictions for DMM in Figures 13f and 13i can be explained by a relatively cold mantle ($<$1300°C) that was previously depleted by ~2% melting (dashed curve). Alternatively, these variations may be consistent with 3-D melt migration, which has been shown to be increasingly important at slower spreading ridges [*Magde and Sparks*, 1997]. In particular, at ultraslow-spreading ridges 3-D melt migration has been invoked to explain extreme along-axis variations in crustal thickness manifest as long amagmatic segments punctuated by widely spaced volcanic centers [e.g., *Dick et al*., 2003; *Standish et al*., 2008]. Future studies that incorporate BG15 into regional 3-D geodynamic models and jointly investigate both major and trace elements would help to distinguish between these scenarios.

5. Caveats and Future Directions

Our goal in formulating BG15 was to provide an improved MORB melting model that could be easily incorporated into geodynamic models to make forward predictions of primary melt compositions. In this way, BG15 can be applied to different regional settings in which high-quality geochemical and geophysical data are available. However, the model described here represents only a first step, which neglects many important aspects of MORB melting. First, although small amounts of H_2O are recognized to have important chemical [*Gaetani and Grove*, 1998; *Asimow and Langmuir*, 2003; *Asimow et al*., 2004; *Cushman et al*., 2004] and geodynamic [*Hirth and Kohlstedt*, 1996; *Braun et al*., 2000] effects on mid-ocean ridge systems, BG15 only considers nominally anhydrous melting. Second, we have not incorporated melting within the garnet regime [e.g., *Grove et al*., 2013] and/or the partitioning of trace elements into the model. Third, there are other important melting processes, such as melting near the exhaustion of clinopyroxene and the partitioning of Cr and Al between the melt and residue that require new experimental data before they can be properly parameterized in melting models. Finally, future geodynamic modeling efforts should seek to directly couple the melting model presented here with the

thermal structure. This would allow feedback between melting and temperature to be more accurately coupled to the flow field through the influences of latent heat removal and melt retention on mantle viscosity. Our hope is that by providing this relative simple model framework, these additions can be added with time (by ourselves or others) and that recalibrations can be easily implemented as additional experimental data become available.

Acknowledgments

We would like to thank C. Till for helping implement her spinel model into BG15. A.Gale graciously provided her compilation of global MORB data that was used for comparison with the melting models in this study. In addition, R. Kinzler, P. Gregg, D. Wanless, and A. Shaw have provided many important insights into the melting processes beneath ridges. This manuscript benefited greatly from thorough and constructive reviews by P. Asimow and E. Klein and Editor M. Walter. Funding was provided by NSF grants OCE-1458201 (M.D.B) and OCE-1457916 (T.L.G) and to M.D.B by the Deep Ocean Exploration Institute at Woods Hole Oceanographic Institution and the Deep Carbon Observatory.

References

Asimow, P., and C. Langmuir (2003), The importance of water to oceanic mantle melting regimes, *Nature*, *421*, 815–820.

Asimow, P., M. Hirschmann, and E. Stolper (1997), An analysis of variations in isentropic melt productivity, *Philos. Trans. R. Soc., London A*, *355*, 255–281.

Asimow, P., M. Hirschmann, and E. Stolper (2001), Calculation of peridotite partial melting from thermodynamic models of mineral and melts. IV. Adiabatic decompression and the composition and mean properties of mid-ocean ridge basalts, *J. Petrol.*, *42*, 963–998.

Asimow, P., J. Dixon, and C. Langmuir (2004), A hydrous melting and fractionation model for mid-ocean ridge basalts: Application to the Mid-Atlantic Ridge near the Azores, *Geochem. Geophys. Geosyst.*, *5*, Q01E16, doi:10.1029/2003GC000568.

Baker, M. B., and E. M. Stolper (1994), Determining the composition of high-pressure mantle melts using diamond aggregates, *Geochim. Cosmochim. Acta*, *58*, 2811–2827, doi:10.1016/0016-7037(94)90116-3.

Baker, M. B., M. M. Hirschmann, M. S. Ghiorso, and E. M. Stolper (1995), Compositions of near-solidus peridotite melts from experiments and thermodynamic calculations, *Nature*, *375*, 308–311, doi:10.1038/375308a0.

Batchelor, G. (1967), *An Introduction to Fluid Mechanics*, Cambridge Univ. Press, Cambridge, U. K.

Behn, M. D., M. S. Boettcher, and G. Hirth (2007), Thermal structure of oceanic transform faults, *Geology*, *35*, 307–310, doi:10.1130/G23112A.1.

Braun, M., G. Hirth, and E. Parmentier (2000), The effects of deep damp melting on mantle flow and melt generation beneath mid-ocean ridges, *Earth Planet. Sci. Lett.*, *176*, 339–356.

Canales, J., J. Collins, J. Escartín, and R. Detrick (2000), Seismic structure across the rift valley of the Mid-Atlantic Ridge at 23°20′N (MARK Area): Implications for crustal accretion processes at slow-spreading ridges, *J. Geophys. Res.*, *105*, 28,411–28,425, doi:10.1029/2000JB900301.

Canales, J., G. Ito, R. Detrick, and J. Sinton (2002), Crustal thickness along the western Galápagos Spreading Center and the compensation of the Galápagos hotspot swell, *Earth Planet. Sci. Lett.*, *203*, 311–327.

Canales, J., R. Detrick, D. Toomey, and W. Wilcock (2003), Segment-scale variations in the crustal structure of 150–300 kyr old fast spreading oceanic crust (East Pacific Rise, 8°15′N–10°5′N) from wide-angle seismic refraction profiles, *Geophys. J. Int.*, *152*, 766–794.

Carbotte, S., M. Nedimovic, J. Canales, G. Kent, A. Harding, and M. Marjanovic (2008), Variable crustal structure along the Juan de Fuca Ridge: Influence of on-axis hot spots and absolute plate motions, *Geochem. Geophys. Geosyst.*, *9*, Q08001, doi:10.1029/2007GC001922.

Chen, Y., and W. Morgan (1990), A nonlinear rheology model for mid-ocean ridge axis topography, *J. Geophys. Res.*, *95*, 17,583–17,604, doi:10.1029/JB095iB11p17583.

Cordery, M. J., and J. Phipps Morgan (1992), Melting and mantle flow beneath a mid-ocean spreading center, *Earth Planet. Sci. Lett.*, *111*, 493–516.

Cushman, B., J. Sinton, G. Ito, and J. Dixon (2004), Glass compositions, plume-ridge interaction, and hydrous melting along the Galapagos Spreading Center, 90.5°W to 98°W, *Geochem. Geophys. Geosyst.*, *5*, Q08E17, doi:10.1029/2004GC000709.

Dalton, C. A., C. H. Langmuir, and A. Gale (2014), Geophysical and geochemical evidence for deep temperature variations beneath mid-ocean ridges, *Science*, *344*, 80–83.

Detrick, R., J. Sinton, G. Ito, J. Canales, M. Behn, T. Blacic, B. Cushman, J. Dixon, D. Graham, and J. Mahoney (2002), Correlated geophysical, geochemical, and volcanological manifestations of plume-ridge interaction along the Galápagos Spreading Center, *Geochem. Geophys. Geosyst.*, *3*(10), 8501, doi:10.1029/2002GC000350.

Dick, H., J. Lin, and H. Schouten (2003), An ultraslow-spreading class of ocean ridge, *Nature*, *426*, 405–412.

Escartín, J., and J. Lin (1998), Tectonic modification of axial crustal structure: Evidence from spectral analyses of residual gravity and bathymetry of the Mid-Atlantic Ridge flanks, *Earth Planet. Sci. Lett.*, *154*, 279–293, doi:10.1016/S0012-821X(97)00194-5.

Forsyth, D. (1993), Crustal thickness and the average depth and degree of melting in fractional melting models of passive flow beneath mid-ocean ridges, *J. Geophys. Res.*, *98*, 16–073–16–079, doi:10.1029/93JB01722.

Gaetani, G. A. (1998), Igneous petrology, *Science*, *282*, 1834–1835.

Gaetani, G. A., and T. L. Grove (1998), The influence of water on melting of mantle peridotite, *Contrib. Mineral. Petrol.*, *131*, 323–346, doi:10.1007/s004100050396.

Gale, A., C. A. Dalton, C. H. Langmuir, Y. Su, and J.-G. Schilling (2013), The mean composition of ocean ridge basalts, *Geochem. Geophys. Geosyst.*, *14*, 489–518, doi:10.1029/2012GC004334.

Gale, A., C. H. Langmuir, and C. A. Dalton (2014), The global systematics of ocean ridge basalts and their origin, *J. Petrol.*, *55*, 1051–1082, doi:10.1093/petrology/egu017.

Ghods, A., and J. Arkani-Hamed (2000), Melt migration beneath mid-ocean ridges, *Geophys. J. Int.*, *140*, 687–697.

Gregg, P. M., M. D. Behn, J. Lin, and T. L. Grove (2009), Melt generation, crystallization, and extraction beneath segmented oceanic transform faults, *J. Geophys. Res.*, *114*, B11102, doi:10.1029/2008JB006100.

Grove, T., R. Kinzler, and W. Bryan (1992), Fractionation of mid-ocean ridge basalt (MORB), in *Mantle Flow and Melt Generation at Mid-Ocean Ridges*, *Geophys. Monogr.*, vol. 71, edited by J. Phipps Morgan, D. Blackman, and J. Sinton, pp. 281–310, AGU, Washington, D. C.

Grove, T. L. (1993), Corrections to expressions for calculating mineral components in "Origin of calc-alkaline series lavas at medicine lake volcano by fractionation, assimilation and mixing" and "Experimental petrology of normal MORB near the kane fracture zone: 22°–25°N, Mid-Atlantic Ridge", *Contrib. Mineral. Petrol.*, *114*, 422–424.

Grove, T. L., E. S. Holbig, J. A. Barr, C. B. Till, and M. J. Krawczynski (2013), Melts of garnet lherzolite: Experiments, models and comparison to melts of pyroxenite and carbonated lherzolite, *Contrib. Mineral. Petrol.*, *166*, 887–910, doi:10.1007/s00410-013-0899-9.

Hebert, L. B., and L. G. J. Montési (2010), Generation of permeability barriers during melt extraction at mid-ocean ridges, *Geochem. Geophys. Geosyst.*, *11*, Q12008, doi:10.1029/2010GC003270.

Herzberg, C., and P. Asimow (2008), Petrology of some oceanic island basalts: PRIMELT2.XLS software for primary magam calculation, *Geochem. Geophys. Geosyst.*, *9*, Q09001, doi:10.1029/2008GC002057.

Herzberg, C., P. D. Asimow, N. Arndt, Y. Niu, C. M. Lesher, J. G. Fitton, M. J. Cheadle, and A. D. Saunders (2007), Temperatures in ambient mantle and plumes: Constraints from basalts, picrites, and komatiites, *Geochem. Geophys. Geosyst.*, *8*, Q02006, doi:10.1029/2006GC001390.

Hirschmann, M., M. Ghiorso, L. Wasylenki, P. Asimow, and E. Stolper (1998), Calculation of peridotite partial melting from thermodynamic models of minerals and melts. I. Review of methods and comparison with experiments, *J. Petrol.*, *39*, 1091–1115.

Hirth, G., and D. Kohlstedt (1996), Water in the oceanic upper mantle: implications for rheology, melt extraction and the evolution of the lithosphere, *Earth Planet. Sci. Lett.*, *144*, 93–108.

Hirth, G., and D. Kohlstedt (2003), Rheology of the upper mantle and the mantle wedge: A view from the experimentalists, in *Inside the Subduction Factory*, *Geophys. Monogr. Ser.*, vol. 138, edited by J. Eiler, pp. 83–105, AGU, Washington, D. C.

Hooft, E. E. E., R. S. Detrick, D. R. Toomey, J. A. Collins, and J. Lin (2000), Crustal thickness and structure along three contrasting spreading segments of the Mid-Atlantic Ridge, 33.5°–35°N, *J. Geophys. Res.*, *105*, 8205–8226, doi:10.1029/1999JB900442.

Ito, G., and P. E. van Keken (2007), Hotspots and melting anomalies, in *Treatise Geophysics*, *Mantle Dyn.*, vol. 7, edited by D. Bercovici, pp. 371–435, Elsevier, Amsterdam.

Jokat, W., J. Kollofrath, W. H. Geissler, and L. Jensen (2012), Crustal thickness and earthquake distribution south of the Logachev Seamount, Knipovich Ridge, *Geophys. Res. Lett.*, *39*, L08302, doi:10.1029/2012GL051199.

Katz, R. (2010), Porosity-driven convection and asymmetry beneath mid-ocean ridges, *Geochem. Geophys. Geosyst.*, *11*, Q0AC07, doi:10.1029/2010GC003282.

Katz, R., M. Spiegelman, and C. Langmuir (2003), A new parameterization of hydrous mantle melting, *Geochem. Geophys. Geosyst.*, *4*(9), 1073, doi:10.1029/2002GC000433.

Katz, R. F., and S. M. Weatherley (2012), Consequences of mantle heterogeneity for melt extraction at mid-ocean ridges, *Earth Planet. Sci. Lett.*, *335–336*, 226–237.

Kelemen, P. B., and E. Aharonov (1998), Periodic formation of magma fractures and generation of layered gabbros in the lower crust beneath oceanic spreading ridges, in *Faulting and Magmatism at Mid-Ocean Ridges*, *Geophys. Monogr. Ser.*, vol. 106, edited by W. Buck et al., pp. 267–289, AGU, Washington, D. C.

Key, K., S. Constable, L. Liu, and A. Pommier (2013), Electrical image of passive mantle upwelling beneath the northern East Pacific Rise, *Nature*, *495*, 499–502, doi:10.1038/nature11932.

Kinzler, R. (1997), Melting of mantle peridotite at pressures approaching the spinel to garnet transition: Application to mid-ocean ridge basalt petrogenesis, *J. Geophys. Res.*, *102*, 853–874, doi:10.1029/96JB00988.

Kinzler, R., and T. Grove (1992a), Primary magmas of mid-ocean ridge basalts, 1. Experiments and Results, *J. Geophys. Res.*, *97*, 6885–6906, doi:10.1029/91JB02840.

Kinzler, R., and T. Grove (1992b), Primary magmas of mid-ocean ridge basalts, 2. Applications, *J. Geophys. Res.*, *97*, 6907–6926, doi:10.1029/91JB02841.

Kinzler, R., and T. Grove (1993), Corrections and further discussion of the primary magmas of mid-ocean ridge basalts, 1 and 2, *J. Geophys. Res.*, *98*, 22,339–22,347, doi:10.1029/93JB02164.

Kinzler, R., and T. L. Grove (1999), Origin of depleted cratonic harzburgite by deep fractional melt extraction and shallow olivine cumulate infusion, in *Proceedings of the 7th International Kimberlite Conference*, edited by J. J. Gurney, pp. 447–453, Red Roof Design, Cape Town.

Klein, E., and C. Langmuir (1987), Global correlations of ocean ridge basalt chemistry with axial depth and crustal thickness, *J. Geophys. Res.*, *92*, 8089–8115, doi:10.1029/JB092iB08p08089.

Kushiro, I. (1975), On the nature of silicate melt and its significance in magma genesis: Regularities in the shift of the liquidus boundaries involving olivine, pyroxene, and silica minerals, *Am. J. Sci.*, *275*, 411–431.

Kushiro, I. (1996), Partial melting of a fertile mantle peridotite at high pressures: An experimental study using aggregates of diamond, in *Earth Processes: Reading the Isotopic Code*, *Geophys. Monogr. Ser.*, vol. 95, edited by A. Basu and S. Hart, pp. 109–122, AGU, Washington, D. C.

Langmuir, C., E. Klein, and T. Plank (1992), Petrological systematics of mid-ocean ridge basalts: Constraints on melt generation beneath ocean ridges, in *Mantle Flow and Melt Generation at Mid-Ocean Ridges*, *Geophys. Monogr. Ser.*, vol. 71, edited by J. Phipps Morgan, D. Blackman, and J. Sinton, pp. 183–280, AGU, Washington, D. C.

Langmuir, C., A. Bezos, S. Escrig, S. Parman, and C. Fisher (2006), Chemical systematics and hydrous melting of the mantle in back-arc basins, in *Back Arc Spreading Systems-Geological, Biological, Chemical and Physical Interactions*, *Geophys. Monogr. Ser.*, vol. 166, edited by D. Christie et al., pp. 87–146, AGU, Washington, D. C.

Langmuir, C. H. (1989), Geochemical consequences of in situ crystallization, *Nature*, *340*, 199–205.

Lee, C.-T. A., P. Luffi, T. Plank, H. Dalton, and W. P. Leeman (2009), Constraints on the depths and temperatures of basaltic magma generation on Earth and other terrestrial planets using new thermobarometers for mafic magmas, *Earth Planet. Sci. Lett.*, *279*, 20–33, doi:10.1016/j.epsl.2008.12.020.

Lissenberg, C., and H. Dick (2008), Melt-rock reaction in the lower oceanic crust and its implications for the genesis of mid-ocean ridge basalt, *Earth Planet. Sci. Lett.*, *271*, 311–325.

Ljones, F., A. Kuwano, R. Mjelde, A. Breivik, H. Shimamura, Y. Murai, and Y. Nishimura (2004), Crustal transect from the North Atlantic Knipovich Ridge to the Svalbard margin west of Hornsund, *Tectonophysics*, *378*, 17–41.

Magde, L., and D. Sparks (1997), Three-dimensional mantle upwelling, melt generation, and melt migration beneath segment slow spreading ridges, *J. Geophys. Res.*, *102*, 20,571–20,583, doi:10.1029/97JB01278.

McKenzie, D., and M. J. Bickle (1988), The volume and composition of melt generated by extension of the lithosphere, *J. Petrol.*, *29*, 625–679.

Montési, L. G. J., and M. D. Behn (2007), Mantle flow and melting underneath oblique and ultraslow mid-ocean ridges, *Geophys. Res. Lett.*, *34*, L24307, doi:10.1029/2007GL031067.

Montési, L. G. J., M. D. Behn, L. B. Hebert, J. Lin, and J. L. Barry (2011), Controls on melt migration and extraction at the ultraslow Southwest Indian Ridge 10°–16°E, *J. Geophys. Res.*, *116*, B10102, doi:10.1029/2011JB008259.

Morgan, W. J. (1971), Convection plumes in the lower mantle, *Nature*, *230*, 42–43.

Morgan, W. J. (1972), Deep mantle convection plumes and plate motions, *AAPG Bull.*, *56*, 203–213.

Navin, D., C. Peirce, and M. Sinha (1998), The RAMESSES experiment—II. Evidence for accumulated melt beneath a slow spreading ridge from wide-angle refraction and multichannel reflection seismic profiles, *Geophys. J. Int.*, *135*, 746–772.

Neumann, G. A., and D. W. Forsyth (1993), The paradox of the axial profile: Isostatic compensation along the axis of the Mid-Atlantic Ridge?, *J. Geophys. Res.*, *98*, 17–891–17–910, doi:10.1029/93JB01550.

Niu, Y., and R. Batiza (1991), An empirical method for calculating melt compositions produced beneath mid-ocean ridges: Application for axis and off-axis (seamounts) melting, *J. Geophys. Res.*, *96*, 21–753–21–777, doi:10.1029/91JB01933.

Niu, Y., and R. Batiza (1993), Chemical variation trends at fast and slow spreading mid-ocean ridges, *J. Geophys. Res.*, *98*, 7887–7902, doi:10.1029/93JB00149.

O'Neill, H., and F. E. Jenner (2012), The global pattern of trace-element distributions in ocean floor basalts, *Nature*, *491*, 698–704.
Phipps Morgan, J. (1987), Melt migration beneath mid-ocean spreading centers, *Geophys. Res. Lett.*, *14*, 1238–1241, doi:10.1029/GL014i012p01238.
Plank, T., and C. Langmuir (1992), Effects of the melting regime on the composition of oceanic crust, *J. Geophys. Res.*, *97*, 19,749–19,770, doi:10.1029/92JB01769.
Plank, T., M. Spiegelman, C. Langmuir, and D. Forsyth (1995), The meaning of "mean F": Clarifying the mean extent of melting an ocean ridges, *J. Geophys. Res.*, *100*, 15,045–15,052, doi:10.1029/95JB01148.
Putirka, K., M. Perfit, F. Ryerson, and M. Jackson (2007), Ambient and excess mantle temperatures, olivine thermometry, and active vs. passive upwelling, *Chem. Geol.*, *241*, 177–206.
Reid, I., and H. Jackson (1981), Oceanic spreading rate and crustal thickness, *Mar. Geophys. Res.*, *5*, 165–171.
Robinson, J., B. Wood, and J. Blundy (1998), The beginning of melting of fertile and depleted peridotite at 1.5 GPa, *Earth Planet. Sci. Lett.*, *155*, 97–111.
Roland, E., M. D. Behn, and G. Hirth (2010), Thermal-mechanical behavior of oceanic transform faults: Implications for the spatial distribution of seismicity, *Geochem., Geophys., Geosyst.*, *11*, Q07001, doi:10.1029/2010GC003034.
Rubin, K., and J. Sinton (2007), Inferences on mid-ocean ridge thermal and magmatic structure from MORB compositions, *Earth Planet. Sci. Lett.*, *260*, 257–276.
Seher, T., W. Crawford, S. Singh, M. Cannat, V. Combier, and D. Dusunur (2010), Crustal velocity structure of the Lucky Strike segment of the Mid-Atlantic Ridge at 37°N from seismic refraction measurements, *J. Geophys. Res.*, *115*, B03103, doi:10.1029/2009JB006650.
Shaw, A. M., M. D. Behn, S. E. Humphris, R. A. Sohn, and P. M. Gregg (2010), Deep pooling of low degree melts and volatile fluxes at the 85°E segment of the Gakkel Ridge: Evidence from olivine-hosted melt inclusions and glasses, *Earth Planet. Sci. Lett.*, *289*(3–4), 311–322, doi:10.1016/j.epsl.2009.11.018.
Shen, Y., and D. W. Forsyth (1995), Geochemical constraints on initial and final depths of melting beneath mid-ocean ridges, *J. Geophys. Res.*, *100*, 2211–2237, doi:10.1029/94JB02768.
Sotin, C., and E. M. Parmentier (1989), Dynamical consequences of compositional and thermal density stratification beneath spreading centers, *Geophys. Res. Lett.*, *16*(8), 835–838, doi:10.1029/GL016i008p00835.
Sparks, D., and E. Parmentier (1991), Melt extraction from the mantle beneath spreading centers, *Earth Planet. Sci. Lett.*, *105*, 368–377.
Sparks, D., E. Parmentier, and J. Phipps Morgan (1993), Three-dimensional mantle convection beneath a segmented spreading center: Implications for along-axis variations in crustal thickness and gravity, *J. Geophys. Res.*, *98*, 21,977–21,995, doi:10.1029/93JB02397.
Spear, F. S. (1993), *Metamorphic Phase Equilibria and Pressure-Temperature-Time Paths*, Mineral. Soc. of Am., Chantilly, Va.
Spear, F. S., J. M. Ferry, and D. Rumble (1982), Analytical formulation of phase equilibria: The Gibb's method, *Rev. Mineral. Geochem.*, *10*, 105–152.
Spera, F. J., and W. A. Bohrson (2001), Energy-constrained open-system magmatic processes I: General model and energy-constrained assimilation and fractional crystallization (EC-AFC) formulation, *J. Petrol.*, *42*, 999–1018.
Spiegelman, M., and D. McKenzie (1987), Simple 2-D models for melt extraction at mid-ocean ridges and island arcs, *Earth Planet. Sci. Lett.*, *83*, 137–152.
Standish, J., H. Dick, P. Michael, W. Melson, and T. O'Hearn (2008), MORB generation beneath the ultraslow spreading Southwest Indian Ridge (9–25°E): Major element chemistry and the importance of process versus source, *Geochem. Geophys. Geosyst.*, *9*, Q05004, doi:10.1029/2008GC001959.
Till, C. B., T. L. Grove, and M. J. Krawczynski (2012), A melting model for variably metasomatized plagioclase and spinel lherzolite, *J. Geophys. Res.*, *117*, B06206, doi:10.1029/2011JB009044.
Tolstoy, M., A. Harding, and J. Orcutt (1993), Crustal thickness on the Mid-Atlantic Ridge: Bull's-eye gravity anomalies and focused accretion, *Science*, *262*, 726–729.
Toomey, D. R., W. S. D. Wilcock, S. C. Solomon, W. C. Hammond, and J. A. Orcutt (1998), Mantle seismic structure beneath the MELT region of the East Pacific Rise from *P* and *S* wave tomography, *Science*, *280*, 1224–1227, doi:10.1126/science.280.5367.1224.
Tormey, D., T. Grove, and W. Bryan (1987), Experimental petrology of normal MORB near the Kane Fracture Zone: 22–25°N, Mid-Atlantic Ridge, *Contrib. Mineral. Petrol.*, *96*, 121–139.
Turcotte, D. L. (1982), Magma migration, *Annu. Rev. Earth Planet. Sci.*, *10*, 397–408, doi:10.1146/annurev.ea.10.050182.002145.
Walter, M. J., and D. C. Presnall (1994), Melting behavior of simplified lherzolite in the system CaO-MgO-Al2O3-SiO2-Na2O from 7 to 35 kbar, *J. Petrol.*, *35*, 329–359, doi:10.1093/petrology/35.2.329.
Wanless, V. D., M. D. Behn, A. M. Shaw, and T. Plank (2014), Variations in melting dynamics and mantle compositions along the Eastern Volcanic Zone of the Gakkel Ridge: Insights from olivine-hosted melt inclusions, *Contrib. Mineral. Petrol.*, *167*, 1–22, doi:10.1007/s00410-014-1005-7.
White, R., D. McKenzie, and R. O'Nions (1992), Oceanic crustal thickness from seismic measurements and rare Earth elements inversions, *J. Geophys. Res.*, *97*, 19,683–19,715, doi:10.1029/92JB01749.
White, R. S., T. A. Minshull, M. J. Bickle, and C. J. Robinson (2001), Melt generation at very slow-spreading oceanic ridges: Constraints from geochemical and geophysical data, *J. Petrol.*, *42*, 1171–1196.
Workman, R. K., and S. R. Hart (2005), Major and trace element composition of the depleted MORB mantle (DMM), *Earth Planet. Sci. Lett.*, *231*(1), 53–72, doi:10.1029/2003GC000568.
Yang, H.-J., R. Kinzler, and T. Grove (1996), Experiments and models of anhydrous, basaltic olivine-plagioclase-augite saturated melts from 0.001 to 10 kbar, *Contrib. Mineral. Petrol.*, *124*, 1–18.